

1 **Susceptibility of Marine Warm Clouds to Aerosols in**  
2 **Different Monsoon Periods over the South China Sea**

3 Yan Liu<sup>1</sup>, Hailing Jia<sup>2</sup>, Yong Han<sup>1\*</sup>

4 <sup>1</sup>Advanced Science & Technology of Space and Atmospheric Physics Group (ASAG), School of  
5 Atmospheric Sciences, Sun Yat-sen University, 519082 Zhuhai, China

6 <sup>2</sup>SRON Space Research Organisation Netherlands, Leiden, The Netherlands

7 \* *Correspondence to:* Yong Han (hany66@mail.sysu.edu.cn)

8

9 **Abstract.**

10 Understanding the susceptibility of warm clouds to aerosol loading, quantified by the aerosol–cloud  
11 interactions (ACI) index, is essential for assessing ACI and their climate impacts. Previous studies have  
12 demonstrated that this susceptibility is strongly modulated by environmental conditions. The South  
13 China Sea (SCS), influenced alternately by the southwest and northeast monsoons, provides a unique  
14 natural laboratory for examining ACI under contrasting thermodynamic and moisture conditions. Using  
15 long-term satellite observations and reanalysis data, we investigate ACI in non-raining warm liquid  
16 clouds over the SCS across three monsoon phases: the southwest monsoon wet period (SWMW),  
17 northeast monsoon wet period (NEMW), and northeast monsoon dry period (NEMD). The robust  
18 Twomey effect is observed across all periods. Shallow stratocumulus clouds show no significant  
19 differences in ACI across periods, whereas deeper cumulus clouds exhibit a progressive increase from  
20 SWMW to NEMW and NEMD, corresponding to transitions from moist convective to dry stable  
21 environments. This variability is likely governed by water-vapor availability and lower-tropospheric  
22 stability (LTS), where stable conditions may enhance ACI through aerosol accumulation, while moist  
23 environments are likely to weaken it via enhanced condensational and coalescence growth. Limitations  
24 of AI as a marine cloud condensation nuclei (CCN) proxy and satellite retrieval biases may affect these  
25 conclusions. These findings reveal the dominant roles of thermodynamic stability and moisture in  
26 regulating ACI over the SCS. The interplay among aerosols, humidity, and stability governs marine  
27 warm-cloud microphysics in tropical monsoon environments, providing observational constraints for  
28 improving the representation of ACI in climate models.

30 **1 Introduction**

31 Aerosol–cloud interactions (ACI) play a crucial role in regulating Earth’s radiative balance and  
32 hydrological cycle by altering cloud microphysical and macrophysical properties (Bellouin et al., 2020;  
33 Jia et al., 2021; Rosenfeld et al., 2019; Stier et al., 2024; Wang et al., 2024c; Zhao et al., 2024). Numerous  
34 studies have demonstrated that ACI are strongly modulated by environmental conditions, such as lower-  
35 tropospheric stability (Chen et al., 2014; Wang et al., 2014), relative humidity (Douglas and L’Ecuyer,

- 删除了: We utilized
- 删除了: datasets to
- 删除了: over the SCS, with a focus on
- 删除了: . Based on large-scale circulation patterns and moisture conditions, the
- 删除了: system over the SCS is categorized into three
- 删除了: the
- 删除了: the
- 删除了: was
- 删除了: three
- 删除了: The
- 删除了: intensity strengthens progressively
- 删除了: further to
- 删除了: the transition
- 删除了: , convectively active
- 删除了: , stably stratified
- 删除了: transition
- 删除了: variations in

54 2019), precipitable water vapor (Qiu et al., 2017; Yuan et al., 2008; Zheng et al., 2022), vertical velocity  
55 (Jia et al., 2022; Su et al., 2010), wind shear (Fan et al., 2009; Kim et al., 2003) , and the vertical overlap  
56 between aerosol and cloud layers (Costantino and Bréon, 2013). However, over the South China Sea  
57 (SCS), a region strongly influenced by pronounced monsoon circulation, the observational evidence of  
58 how ACI respond to variations in thermodynamic and moisture conditions remains limited.

59 The SCS, one of the world’s largest marginal seas, provides a unique natural laboratory for investigating  
60 ACI under the alternating influence of two opposing monsoon systems. The SCS experiences a  
61 pronounced seasonal reversal of wind regimes, characterized by a warm, moist southwest monsoon  
62 during boreal summer and a cool, dry northeast monsoon during boreal winter (Wang et al., 2009).  
63 During the southwest monsoon period, the marine boundary layer over the northern SCS becomes  
64 unstable, with enhanced air–sea temperature differences and surface turbulent heat fluxes that intensify  
65 vertical mixing and deepen the boundary layer while reducing wind shear (Peng et al., 2016). Rainfall  
66 during this period is primarily governed by warm-cloud microphysical processes and vapor convergence-  
67 driven condensation (Wang et al., 2007). In contrast, during the northeast monsoon period, cold surges  
68 associated with the East Asian winter monsoon substantially modify the SCS boundary-layer structure  
69 by enhancing surface turbulent fluxes, deepening the mixed layer, and strengthening the inversion that  
70 promotes extensive low-cloud development (Wang et al., 2024a). The SCS is also a region that is  
71 simultaneously affected by various types of aerosols from industrial emissions, shipping activities, and  
72 biomass burning. It has been shown that those aerosols substantially modify the microphysical structure  
73 of marine boundary layer clouds over the SCS by increasing small droplet concentrations and suppressing  
74 midsize droplets near cloud base (Miller et al., 2023). Recent shipborne observations further reveal that  
75 aerosol sources over the SCS exhibit distinct seasonal contrasts, being dominated by continental outflow  
76 from mainland Southeast Asia during the southwest monsoon and by pollution plumes transported from  
77 continental China during the northeast monsoon (Ou et al., 2025). Yet, how these contrasting aerosol and  
78 meteorological regimes modulate ACI, particularly for warm non-raining clouds, remains poorly  
79 quantified.

80 Quantifying ACI is essential for constraining their climatic impacts. According to the Sixth Assessment  
81 Report of the Intergovernmental Panel on Climate Change (Douville et al., 2023) , the effective radiative

82 forcing associated with ACI ( $ERF_{aci}$ ) is estimated to be  $-0.84 \text{ W m}^{-2}$  globally, with a wide 5–95%  
 83 confidence range from  $-1.45 \text{ W m}^{-2}$  to  $-0.25 \text{ W m}^{-2}$ , dominating the overall uncertainty in total aerosol  
 84 effective radiative forcing, which ranges between  $-1.7$  and  $-0.4 \text{ W m}^{-2}$ .  $ERF_{aci}$  may be further  
 85 decomposed into two components: the instantaneous radiative forcing due to ACI, also known as the  
 86 Twomey effect ( $RF_{aci}$ , Twomey, 1977, 1974), and rapid adjustments (Ackerman et al., 2004; Albrecht,  
 87 1989; Bellouin et al., 2020). To quantify the cloud response to aerosol perturbations, Feingold et al. (2001)  
 88 proposed the ACI index ( $ACI_r$  and  $ACI_{Nd}$ ), which has since become a widely used metric for evaluating  
 89 the strength of the Twomey effect in both satellite and in-situ studies, defined as:

90 
$$ACI_r = -d \ln r / d \ln \alpha \quad (1)$$

91 
$$ACI_{Nd} = d \ln N_d / d \ln \alpha \quad (2)$$

92 where  $r$  and  $N_d$  denote the cloud effective radius and droplet number concentration, respectively, and  $\alpha$   
 93 is an aerosol proxy (e.g., AOD, AI, or NCCN). In this study, AI is employed as the aerosol proxy in the  
 94 calculation of ACI.  $ACI_{Nd}$  is more recently also referred to as the  $N_d$  susceptibility to aerosols (Ma et al.,  
 95 2018a, b).

96 Although many studies have examined the environmental modulation of ACI over both oceanic and  
 97 continental regions (Fan et al., 2016; Jia et al., 2019, 2022; Jia and Quaas, 2023; Seinfeld et al., 2016;  
 98 Sorooshian et al., 2019; Wall et al., 2022; Wang et al., 2024d), such processes remain poorly constrained  
 99 over the SCS. The pronounced seasonal reversal of monsoon circulation in this region creates highly  
 100 contrasting thermodynamic and moisture conditions, along with differing aerosol regimes, which  
 101 together exert distinct influences on cloud microphysics and modulate the ACI processes. Therefore, this  
 102 study aims to provide a comprehensive assessment of ACI in non-raining warm clouds over the SCS  
 103 under different monsoon regimes. Long-term multi-satellite and reanalysis datasets from July 2002 to  
 104 February 2023 are integrated to characterize variations in aerosol, cloud, and environmental properties  
 105 across the southwest monsoon wet (SWMW), northeast monsoon wet (NEMW), and northeast monsoon  
 106 dry (NEMD) phases, and to quantitatively evaluate the corresponding ACI responses. Particular attention  
 107 is given to understanding how variations in water vapor availability and lower-tropospheric stability  
 108 (LTS) influence the sensitivity of cloud microphysical responses to aerosol perturbations.

删除了:  $ACI_r = -d \ln r / d \ln N_{CCN}$

域代码已更改

删除了:  $ACI_{Nd} = d \ln N_d / 3d \ln N_{CCN}$

域代码已更改

删除了:  $N_{CCN}$  represents a proxy for cloud condensation nuclei (CCN) number concentration.

113 The paper is organized as follows. Section 2 describes the datasets and method used in this study. The  
 114 main findings and related discussions are presented in Section 3. Section 4 summarizes the key findings  
 115 and conclusions.

116 **2 Data and Methods**

117 This study employs long-term, multi-source datasets to investigate ACI over the SCS. The cloud  
 118 properties are derived from the Clouds and the Earth’s Radiant Energy System (CERES)–Moderate  
 119 Resolution Imaging Spectroradiometer (MODIS) Edition 4 Level-3 product (SSF1deg, Aqua, daytime).

120 Cloud droplet number concentration (Nd) data are obtained from a community-standard gridded dataset  
 121 provided by Gryspeerdt et al. (2022). Aerosol optical properties is obtained from the Modern-Era  
 122 Retrospective analysis for Research and Applications, Version 2 (MERRA-2). Meteorological fields are  
 123 taken from the European Centre for Medium-Range Weather Forecasts (ECMWF) fifth-generation  
 124 reanalysis (ERA5). Precipitation data are provided by the Integrated Multi-satellite Retrievals for GPM  
 125 (IMERG) Version 7 Final Run, and sea surface temperature (SST) data are obtained from the National  
 126 Oceanic and Atmospheric Administration (NOAA) Optimum Interpolation (OI) SST, version 2. The  
 127 definitions of the monsoon regimes and the analyses of large-scale circulation, aerosol, and cloud  
 128 properties are conducted at their native spatial resolutions. For aerosol–cloud collocation, AOD, AI, and  
 129 ERA5 meteorological fields used in the calculation of ACI and environmental stratification are regridded  
 130 to a common 1° × 1° grid using bilinear interpolation with the Climate Data Operators (CDO, remapbil).

131 **Table 1: Overview of datasets used in this study.**

Parameter	Data Source	Spatial Resolution	Temporal Resolution	Data Range
Cloud Effective Radius	CERES–MODIS	1° × 1°	daily	Jul 2002 –
Cloud Optical Thickness	V04 SSF1deg			Feb <del>2020</del>
Cloud-top Temperature	(Aqua, daytime)			
Cloud-top Pressure				
Liquid Cloud Area Fraction				
Liquid Water Path				
<u>Cloud droplet number concentration</u>	<u>Gryspeerdt et al. (2022)</u>	<u>1° × 1°</u>	<u>daily</u>	<u>Jul 2002 – Feb 2020</u>
Total aerosol extinction (550 nm)	AOT MERRA-2	0.5° × 0.625°	daily	Jul 2002 – Feb <del>2020</del>

删除了: Aerosol information is obtained from the Modern-Era Retrospective analysis for Research and Applications, Version 2 (MERRA-2). Meteorological fields are taken from the European Centre for Medium-Range Weather Forecasts (ECMWF) fifth-generation reanalysis (ERA5). Precipitation data are provided by the Integrated Multi-satellite Retrievals for GPM (IMERG) Version 7 Final Run, and sea surface temperature (SST) data are obtained from the National Oceanic and Atmospheric Administration (NOAA) Optimum Interpolation (OI) SST, version 2.

删除了: 2023

删除了: 2023

Total aerosol Ångström parameter (470–870 nm)						
Specific Humidity	ERA5		0.25°	×	daily	Jul 2002 –
Temperature			0.25°			Feb <del>2020</del>
horizontal wind components						
mean sea level pressure						
Precipitation	IMERG	V07	0.1° × 0.1°		30 min	Jul 2002 –
	Final					Feb <del>2020</del>
Sea Surface Temperature	NOAA OI	SST	1° × 1°		monthly	Jul 2002 –
	V2					Feb <del>2020</del>

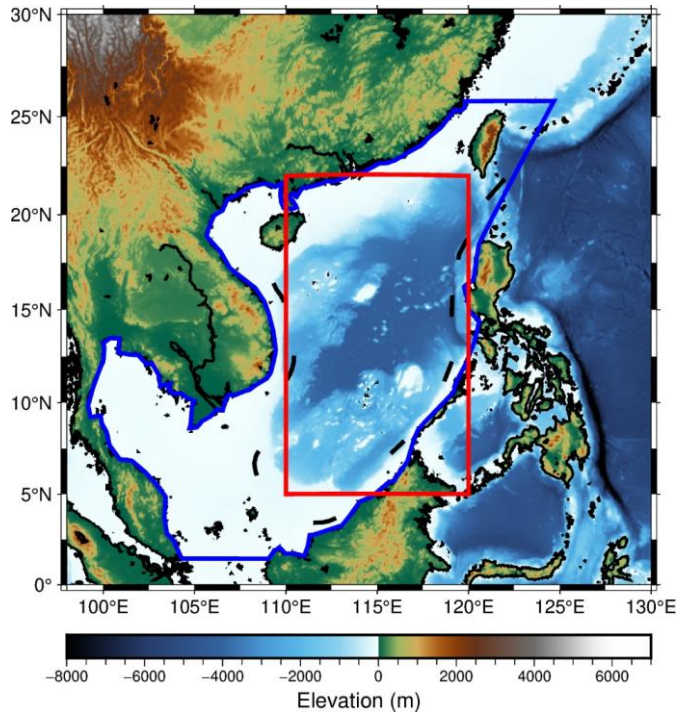
删除了: 2023

删除了: 2023

删除了: 2023

143 **2.1 Study Area**

144 SCS is one of the world’s largest marginal seas, characterized by complex air–sea interactions and a  
145 pronounced seasonal reversal of wind systems (Wang et al., 2009). This region is strongly influenced by  
146 the Asian monsoon circulation, exhibiting distinct southwest and northeast monsoon regimes that  
147 profoundly modulate its thermodynamic and dynamic environments (Zheng et al., 2025). These  
148 alternating monsoon circulations govern the regional aerosol loading (Ou et al., 2025), boundary-layer  
149 structure (Chen et al., 2025; Peng et al., 2016; Wang et al., 2024a), and cloud microphysical processes  
150 (Miller et al., 2023; Wang et al., 2024b), making the SCS an ideal natural laboratory for investigating  
151 ACI under contrasting meteorological conditions. In this study, the analysis domain (blue polygon in Fig.  
152 1) encompasses the entire SCS, including both coastal and open-ocean areas, to capture the spatial  
153 variability of aerosol, cloud, and environmental parameters. The red box in Fig. 1 delineates the  
154 subregion (3°–22° N, 110°–120° E) used for defining the monsoon regimes following Wang et al. (2004).



158

159 **Figure 1: Study region and monsoon classification over the South China Sea. The blue polygon indicates the**  
 160 **study domain, while the red box marks the region used for defining the monsoon regimes.**

161 **2.2 Cloud Remote Sensing Products**

162 Cloud retrievals used in this study are derived from the Moderate Resolution Imaging Spectroradiometer  
 163 (MODIS) aboard the Aqua satellite, which has an equatorial crossing time of approximately 1:30 p.m.  
 164 local time. The MODIS cloud products analysed are obtained from the Clouds and the Earth's Radiant  
 165 Energy System (CERES) MODIS (CERES–MODIS hereafter) Edition 4 (Minnis et al., 2011a, 2021)  
 166 Single Scanner Footprint (SSF) daily products (Level 3,  $1^\circ \times 1^\circ$  grid resolution), which provide  
 167 physically consistent cloud and radiative properties based on synergistic MODIS and CERES  
 168 observations. The CERES–MODIS cloud retrievals have been extensively validated (Minnis et al.,  
 169 2011b; Yost et al., 2021) and have been widely employed in studies of ACI (Jia et al., 2021; Painemal,  
 170 2018). CERES–MODIS Edition 4 SSF cloud parameters utilized here include cloud optical depth ( $\tau$ ),  
 171 cloud effective radius (CER), cloud-top temperature (CTT), cloud-top pressure (CTP), liquid cloud area

172 fraction (LCAF), and liquid water path (LWP). CER is retrieved from the 3.7- $\mu\text{m}$  channel, which is less  
 173 affected by retrieval biases than its 2.1- and 1.6- $\mu\text{m}$  counterparts (Grosvenor et al., 2018).  
 174  $N_d$  used in this study is obtained from the community-standard gridded dataset of Gryspeerdt et al. (2022),  
 175 which provides  $1^\circ \times 1^\circ$  Level-3  $N_d$  products derived from pixel-level MODIS Collection 6.1 retrievals.  
 176 In this dataset,  $N_d$  is first estimated at the native MODIS pixel scale using retrieved cloud optical  
 177 thickness and cloud effective radius, and then aggregated to a common grid using established sampling  
 178 strategies to ensure robustness and consistency. The  $N_d$  retrievals are based on the adiabatic cloud  
 179 assumption and are subject to strict quality control procedures, including screening for optically thin  
 180 clouds, large solar zenith angle and viewing zenith angle conditions, sub-pixel heterogeneity, and  
 181 potential retrieval contamination. Only single-layer liquid cloud scenes are retained. This dataset has  
 182 been evaluated against observations and is widely used in aerosol–cloud interaction studies (e.g., Jia et  
 183 al., 2024; Wall et al., 2023). In this study, we use the  $N_d$  G18\_37 product from this community-standard  
 184 dataset.

### 185 2.3 Aerosol Optical Properties

186 Aerosol properties used in this study are obtained from the Modern-Era Retrospective Analysis for  
 187 Research and Applications, Version 2 (MERRA-2, Gelaro et al., 2017), which assimilates a wide range  
 188 of satellite observations to provide a physically consistent representation of global aerosol distributions.  
 189 The MERRA-2 aerosol dataset used here includes the total aerosol extinction (AOD, 550 nm) and the  
 190 total aerosol Ångström parameter (AE, 470-870 nm), with a spatial resolution of  $0.5^\circ \times 0.625^\circ$  and a  
 191 temporal resolution of 1 hour. To ensure spatiotemporal consistency with the CERES–MODIS cloud  
 192 products, the MERRA-2 aerosol fields at 14:00 local solar time (LST), closest to the Aqua overpass  
 193 (~13:30 LST), were regridded to a  $1^\circ \times 1^\circ$  grid. AOD represents the column-integrated aerosol extinction,  
 194 whereas AE characterizes the wavelength dependence of AOD and is commonly used as an indicator of  
 195 aerosol particle size. A higher AE generally indicates dominance of fine-mode aerosols, while a lower  
 196 AE suggests coarse-mode particles. The aerosol index (AI) is defined as the product of AOD and AE:

$$197 \quad \text{AI} = \text{AOD} \times \text{AE} \quad (3)$$

删除了: Following previous studies that derived  $N_d$  from the CERES–MODIS L3 product (Dadashazar et al., 2021; Painemal et al., 2021) using an adiabatic formulation (Grosvenor et al., 2018),  $N_d$  was calculated as:

$$\text{删除了: } N_d = \frac{\sqrt{5}}{2\pi k} \left( \frac{f_{ad} C_w \tau}{Q_{ext} \rho_w r_e^5} \right)^{1/2} \quad (3)$$

Where,  $k$  is a constant factor that relates volume radius to CER and is assumed to be 0.8 over the ocean (Martin et al., 1994),  $\rho_d$  is the liquid water density,  $\tau$  is cloud optical depth,  $r_e$  is cloud effective radius,  $Q_{ext}$  is the dimensionless extinction efficiency factor (assumed to be 2 for liquid droplets),  $f_{ad}$  is the adiabatic fraction, set to 0.7, and  $C_w$  is the adiabatic lapse rate of liquid water content calculated from the CTT and CTP (Braun et al., 2018) obtained from CERES–MODIS:

$$C_w = \left[ \frac{(\epsilon + w_s) w_s l_v \Gamma_m}{R_d T^2} - \frac{g w_s P}{(P - e_s) R_d T} \right] \rho_d \quad (4)$$

where,  $R_d$  is the ideal gas constant for dry air,  $\epsilon$  is the ratio of the gas constants for dry air and water vapor,  $w_s$  is the saturation mixing ratio,  $l_v$  is the latent heat of vaporization,  $T$  is the CTT,  $\Gamma_m$  is the moist adiabatic lapse rate (as defined in the American Meteorological Society’s Glossary),  $g$  is the gravitational acceleration,  $P$  is the CTP,  $e_s$  is the saturation vapor pressure of water, and  $\rho_d$  is the density of dry air. CTT was used to calculate  $e_s$  and  $l_v$ , while both CTT and CTP were used to calculate  $w_s$ ,  $\Gamma_m$ , and  $\rho_d$ .

删除了:  $\text{AI} = \text{AOD} \times \text{AE} \quad (5)$

域代码已更改

221 AI, in comparison to AOD, is considered a better parameter for representing aerosols in ACI studies,  
222 because it incorporates information on aerosol particle size, which is critical for cloud droplet activation  
223 and microphysical properties (Ma et al., 2018b; Nakajima et al., 2001). Therefore, AI is employed in this  
224 study as the aerosol proxy in the calculation of ACI.

#### 225 **2.4 Atmospheric Parameters of Weather Fields**

226 Atmospheric fields were obtained from the fifth-generation ECMWF reanalysis (ERA5, Hersbach et al.,  
227 2020). ERA5 assimilates a comprehensive suite of ground-based and satellite observations through a  
228 state-of-the-art four-dimensional variational data assimilation system, offering physically consistent and  
229 dynamically balanced representations of the atmosphere. The dataset used here includes three-  
230 dimensional fields of specific humidity and horizontal wind components (U and V) at all standard  
231 pressure levels, temperature at 1000 and 700 hPa, and mean sea level pressure. The daily mean specific  
232 humidity and wind speed at 850 hPa were used to distinguish the three periods over the SCS (Wang et  
233 al., 2004). Wind and humidity fields at all pressure levels were analysed to characterize the large-scale  
234 atmospheric circulation and vertical moisture structure during these periods. The 1000 hPa specific  
235 humidity was employed as a proxy for the ambient water vapor available to warm clouds (Dadashazar et  
236 al., 2020). Temperatures at 1000 and 700 hPa were used to compute the LTS, which quantifies the  
237 thermodynamic stability of the lower atmosphere (Klein and Hartmann, 1993), as follows:

238

$$239 \quad \begin{aligned} LTS &= \theta_{700hPa} - \theta_{1000hPa} \\ \theta &= T \left( \frac{P_{00}}{P} \right)^{\frac{R}{C_p}} \end{aligned} \quad (4)$$

240 where  $\theta_{700}$  and  $\theta_{1000}$  denote the potential temperatures at 700 and 1000 hPa, respectively,  $P_{00}$  is the  
241 standard reference pressure (typically 1000 hPa),  $P$  is the pressure at a given level,  $R$  is the gas constant  
242 for dry air, and  $C_p$  is the specific heat capacity of dry air at constant pressure. To ensure spatiotemporal  
243 consistency with the aerosol and cloud parameters, both the 1000 hPa specific humidity and LTS at 14:00  
244 LST were regridded to a  $1^\circ \times 1^\circ$  grid. Sea surface temperature (SST) was obtained from the National  
245 Oceanic and Atmospheric Administration (NOAA) Optimum Interpolation SST, version 2 (OI SST v2,

246 Reynolds et al., 2002), which incorporates both in-situ and satellite observations and provides monthly  
247 fields at  $1^\circ \times 1^\circ$  resolution.

## 248 **2.5 Precipitation Data**

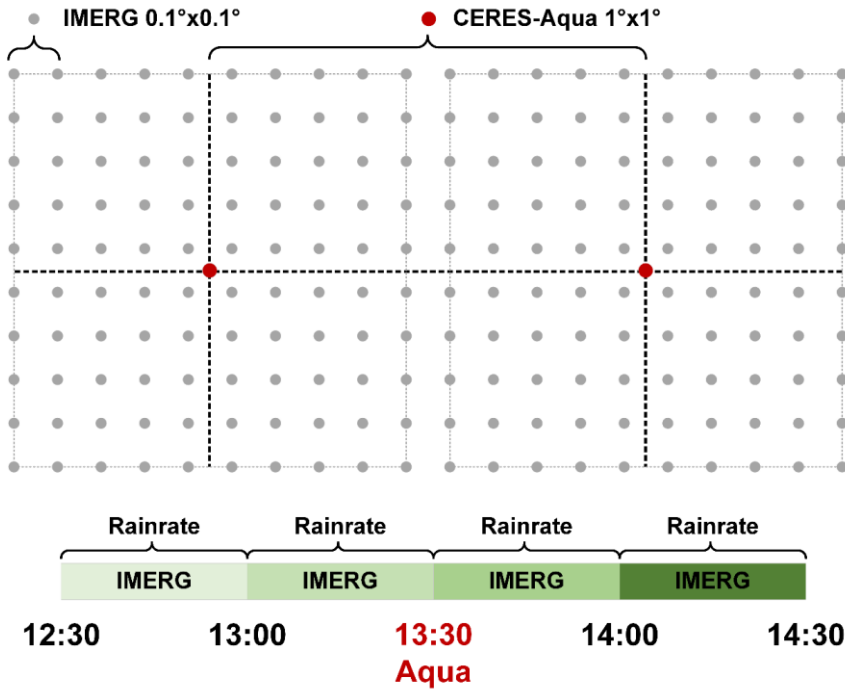
249 Precipitation data were obtained from the Integrated Multi-satellite Retrievals for GPM (IMERG)  
250 Version 07 Final run. IMERG is the flagship precipitation product of the Global Precipitation  
251 Measurement (GPM) mission, a collaborative effort between NASA and JAXA (Huffman et al., 2023).  
252 The IMERG algorithm calibrates, merges, and interpolates precipitation estimates from the constellation  
253 of Low Earth Orbit (LEO) passive microwave (PMW) radiometers onboard GPM satellites. These  
254 estimates are subsequently integrated with geostationary satellite infrared observations, particularly in  
255 regions with sparse PMW coverage, to produce a global precipitation product with  $0.1^\circ$  spatial and 30-  
256 minute temporal resolutions (Huffman et al., 2020; Watters et al., 2021). IMERG precipitation data,  
257 owing to its global coverage and high spatiotemporal resolution, have been widely adopted by the  
258 research community (Dezfuli et al., 2017; Durden, 2024; Hayden et al., 2023; Tan et al., 2019a; Watters  
259 et al., 2021; Watters and Battaglia, 2019; Zhang and Wang, 2024; Zhu et al., 2024). Consequently,  
260 IMERG V07 Final Run PrecipitationCal, the gauge-calibrated multi-satellite product, is used here to  
261 determine whether precipitation occurred within each CERES–MODIS grid cell.

## 262 **2.6 Data Quality Control**

263 To minimize the influence of satellite retrieval biases when investigating ACI, a rigorous quality-control  
264 procedure was applied to the CERES–MODIS cloud dataset following the method of Saponaro et al.  
265 (2017). The selection criteria were as follows:

- 266 1. Only liquid-phase warm clouds were retained, identified by a cloud-phase flag of “liquid” and  $CTT >$   
267  $273\text{ K}$ .
- 268 2. To reduce the impact of large-scale cloud-macrophysical variability and highlight microphysical  
269 processes, only clouds with CTP between 650 and 950 hPa were selected.
- 270 3. Thin clouds with  $\tau < 5$  were excluded to minimize retrieval uncertainty.
- 271 4. A threshold of  $<0.2\text{ mm h}^{-1}$  was adopted to identify IMERG non-raining cases, following Tan et al.  
272 (2019b). The IMERG precipitation data were first collocated onto CERES–MODIS  $1^\circ \times 1^\circ$  grid

273 cells. A grid cell was then classified as non-raining when all IMERG sub-pixels within the 13:00–  
 274 13:30 and 13:30–14:00 local time intervals recorded precipitation rates below  $0.2 \text{ mm h}^{-1}$ , as  
 275 illustrated in Fig. 2.



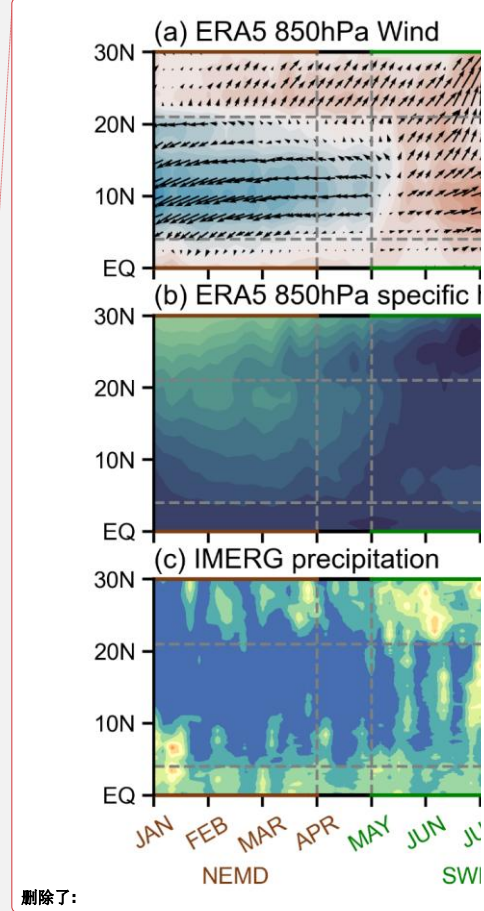
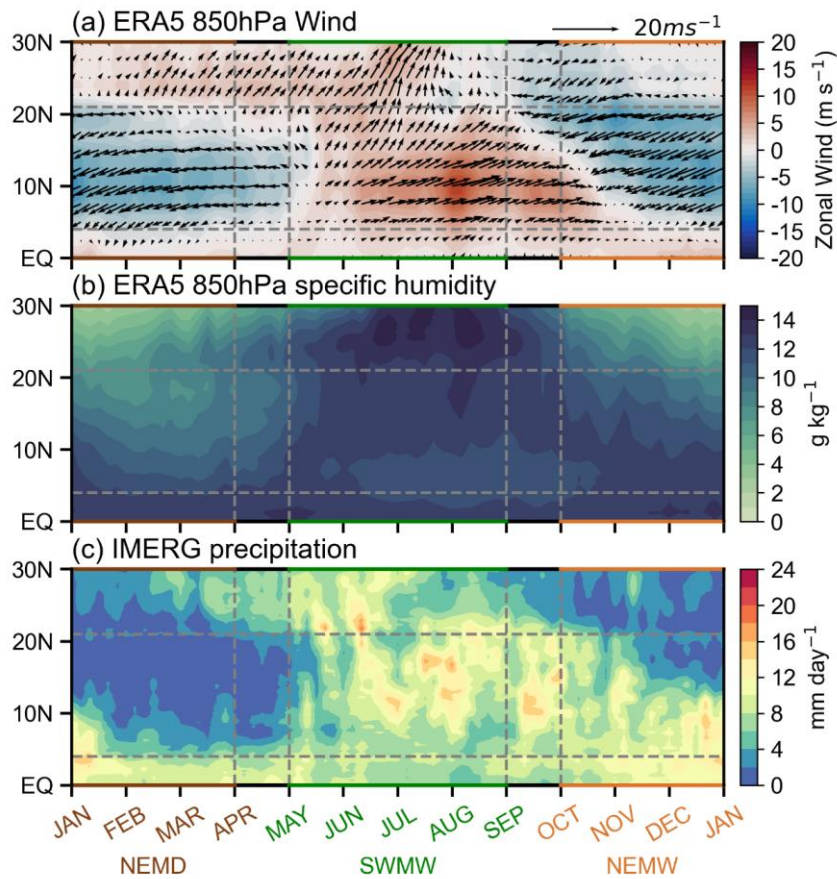
276  
 277 **Figure 2: Schematic illustration of the procedure used to identify non-raining CERES–MODIS grid cells**  
 278 **based on IMERG V07 Final Run PrecipitationCal.**

279 **3 Result**

280 **3.1 Definition of Monsoon Periods over the South China Sea**

281 ACI are strongly modulated by environmental factors such as humidity, vertical wind velocity, and  
 282 atmospheric stability (Zhu et al., 2022). Therefore, considering the prevailing atmospheric conditions is  
 283 crucial when examining their variability. The atmospheric environment over the SCS exhibits distinct  
 284 characteristics under the influence of the southwest monsoon and the northeast monsoon. A distinctive  
 285 feature of the SCS summer monsoon is its nearly simultaneous onset across a broad latitudinal range  
 286 ( $3^{\circ}$ – $22^{\circ}$ N) (Wang et al., 2004). On top of the previous studies that defined monsoon periods over the  
 287 SCS based on wind direction (Wang et al., 2004, 2009), we further incorporated precipitation and specific

288 humidity within this 3-22°N band (the red box in Fig. 1) to classify the study periods into three regimes:  
289 the southwest monsoon wet period (SWMW), the northeast monsoon dry period (NEMD), and the  
290 northeast monsoon wet period (NEMW). As shown in Fig. 3, the SCS is dominated by the southwest  
291 monsoon from May to August, during which specific humidity reaches its maximum and precipitation is  
292 strongest. From October to December, the northeast monsoon prevails, accompanied by relatively high  
293 specific humidity and intense precipitation. During January to March, the SCS remains under the  
294 influence of the northeast monsoon, but specific humidity is at its lowest and precipitation is minimal,  
295 representing a dry period. Accordingly, we defined May–August as SWMW, October–December as  
296 NEMW, and January–March as NEMD. These three periods not only reflect significant differences in  
297 atmospheric circulation and moisture conditions, along with aerosol regimes over the SCS, but also  
298 provide distinct environmental backgrounds for ACI, which may influence their characteristics and  
299 intensity.



300  
 301 **Figure 3: Time-latitude distribution of the (a) ERA5 climatological pentad mean 850 hPa zonal wind (Jul**  
 302 **2002–Feb 2020) and (b) ERA5 pentad mean 850 hPa specific humidity (Jul 2002–Feb 2020) and (c) IMERG**  
 303 **pentad mean precipitation (Jul 2002–Feb 2020). The data are averaged over the longitude bands between**  
 304 **110E and 120E across the SCS. The arrows in (a) indicates 850hPa horizontal winds.**

305 **3.2 Atmospheric conditions and Aerosol–Cloud properties during the Three Periods**

306 **3.2.1 Atmospheric Circulation and Sea Surface Temperature**

307 The Hadley circulation over the SCS is modulated by the Asian monsoon system and the seasonal  
 308 variation of solar radiation. Fig. 4a shows that during the SWMW period, the SCS is dominated by  
 309 ascending motion, which is associated with the presence of the Intertropical Convergence Zone (ITCZ)  
 310 over the region. During the NEMW period, the Hadley circulation shifts southward and the subtropical  
 311 high is established over the northern SCS (Fig. 4e). As a result, subsidence dominates the northern part

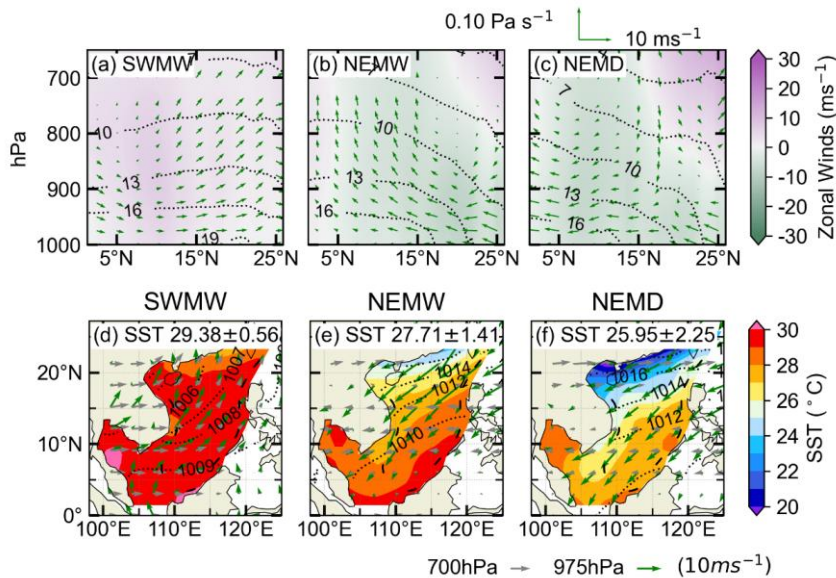
删除了:

删除了: 2023

删除了: 2023

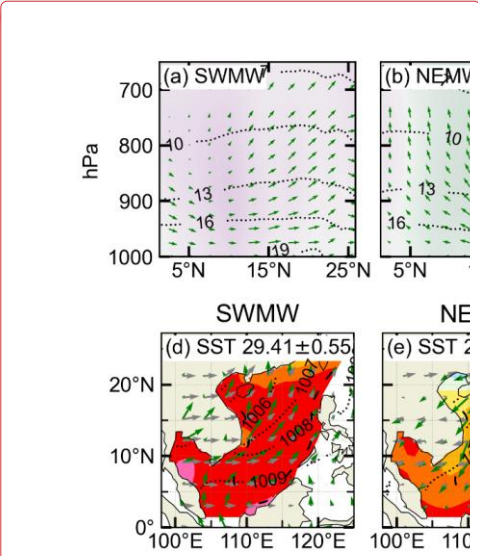
删除了: 2023

316 of the region, whereas ascending motion occurs over the equatorial southern part (Fig. 4b). During the  
 317 NEMD period, as the Hadley circulation continues to shift southward, the subtropical high dominates  
 318 the SCS (Fig. 4f), leading to prevailing subsidence over the region (Fig. 4c). As shown in Figs. 4a-c, the  
 319 water vapor content over the SCS gradually decreases from the SWMW period to the NEMW period and  
 320 further to the NEMD period. During the SWMW period, the winds over the SCS are predominantly  
 321 westerly. In contrast, during both the NEMW and NEMD periods, the winds are mainly easterly.  
 322 Additionally, a westerly jet is present at upper levels over the northern SCS. These features show that  
 323 the SCS exhibits distinct vertical circulation, moisture, and wind patterns under different monsoon  
 324 conditions.



325  
 326 **Fig. 4.** Zonally averaged cross section of the atmospheric circulation from ERA5 (Jul 2002–Feb 2020) for the  
 327 domain bounded between 110°E and 120°E during (a) the southwest monsoon wet period, (b) the northeast  
 328 monsoon wet period, and (c) the northeast monsoon dry period. Meridional and pressure velocity are denoted  
 329 by arrows (↑ indicates upward motion), whereas colors indicate the zonal wind component. Black contour is  
 330 specific humidity. Panels (d–f) show the corresponding overview of meteorological conditions and SST over  
 331 the SCS region. Color shades represent SST from OISST (Jul 2002–Feb 2020), black contour is sea level  
 332 pressure from ERA5 (Jul 2002–Feb 2020), and arrows are near-surface wind speed at 975 hPa (green) and  
 333 that at 700 hPa (gray) from ERA5 (Jul 2002–Feb 2020).

334 The SCS exhibits contrasting large-scale circulation patterns between the southwest and northeast  
 335 monsoon periods, as shown in Figs. 4d–f. During the SWMW period, the SCS is influenced by tropical



删除了:

删除了: 2023

删除了: 2023

删除了: 2023

删除了: 2023

341 and equatorial maritime air masses, with prevailing southwesterlies over the region (Martin and Howland,  
342 1982), whereas during the northeast monsoon, winter airflows originating from Siberia and the  
343 Mongolian Plateau result in prevailing northeasterlies (Liu et al., 2024). These opposite prevailing wind  
344 directions play a crucial role in modulating the transport pathways of continental pollutants into the SCS.  
345 Specifically, air masses originating from the Indochinese Peninsula and surrounding Southeast Asian  
346 land regions are the primary sources of pollutants transported into the SCS (Miller et al., 2023; Ou et al.,  
347 2025; Sun et al., 2023; Zhang et al., 2019), whereas during the northeast monsoon, continental emissions  
348 from China may be carried southward into the region(Xiao et al., 2017; Yuan et al., 2024; Zheng et al.,  
349 2023).

350 Figures 4d–f show that the area-averaged SST over the SCS is highest during the SWMW period ( $29.38$   
351  $\pm 0.56$  °C), lower during the NEMW period ( $27.71 \pm 1.41$  °C), and lowest during the NEMD period  
352 ( $25.95 \pm 2.25$  °C), with variations consistent with those of specific humidity. During the southwest  
353 monsoon, the SST gradient across the SCS is relatively small, whereas during the northeast monsoon,  
354 SST decreases with increasing latitude (Wu et al., 2020), and a cold water band forms along the coastal  
355 region near mainland China (Chen and Hu, 2023). Higher SST promotes strong latent and sensible heat  
356 fluxes, which in turn enhance the atmospheric moisture content over the region (Lee and Park, 2022;  
357 Zhang et al., 1995). Consequently, SST and atmospheric moisture exhibit consistent variations across  
358 the three periods. In addition, during the northeast monsoon, both the SST (Figs. 4e–f) and atmospheric  
359 moisture (Figs. 4b–c) decrease with increasing latitude, showing similar latitudinal gradients.

### 360 3.2.2 Aerosol and cloud properties

361 The area-averaged aerosol values over the SCS exhibit clear differences among the three periods (Fig.  
362 5). The lowest values occur during the SWMW period, with  $AOD = 0.17 \pm 0.04$  and  $AI = 0.16 \pm 0.06$ .  
363 Higher values are observed during the NEMW period, with  $AOD = 0.23 \pm 0.08$  and  $AI = 0.20 \pm 0.13$ ,  
364 whereas the NEMD period shows the highest values, with  $AOD = 0.27 \pm 0.14$  and  $AI = 0.30 \pm 0.23$ ,  
365 indicating different aerosol sources. Significant differences in aerosol distribution are also observed  
366 between the southwest and northeast periods. During the southwest period, higher aerosol values are  
367 found in the northern SCS near mainland China and in the southwestern SCS near Malaysia. During the  
368 northeast period, aerosol values exhibit a pronounced gradient, forming a coastal band that decreases

删除了: 41

删除了: 55

删除了: 75

删除了: 39

删除了: 98

删除了: 22

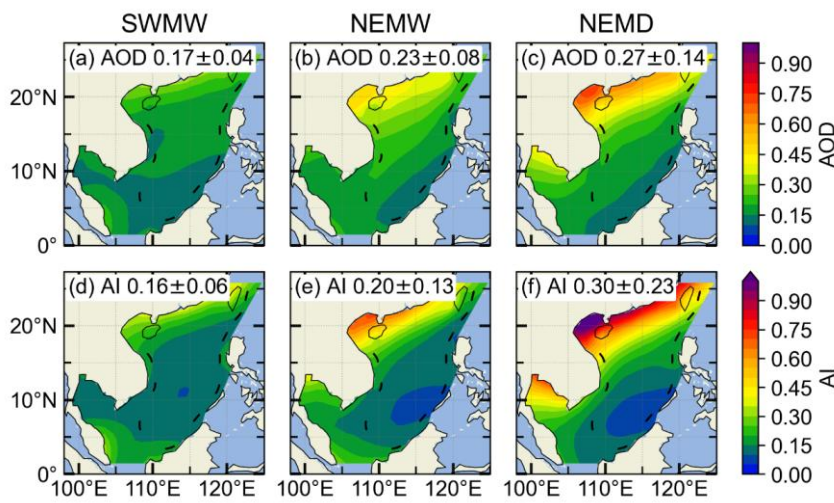
删除了: 12

删除了: 26

删除了: 29

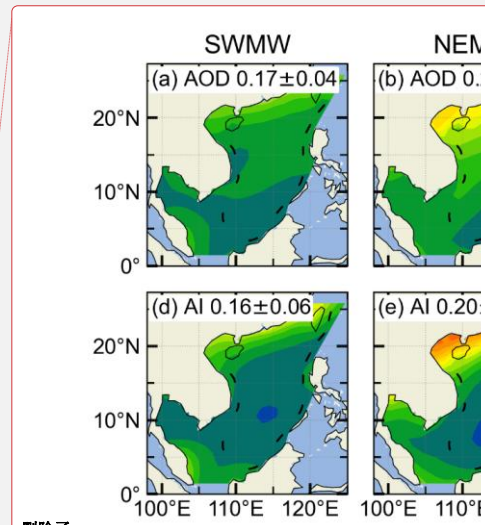
删除了: 22

379 with increasing distance from the shoreline (Tu et al., 2021). Compared with AOD, AI incorporates  
 380 aerosol size information and is therefore considered a more suitable proxy for cloud condensation nuclei  
 381 in studies of ACI (Nakajima et al., 2001). Over the northern SCS near mainland China, AI values are  
 382 larger than AOD, indicating that aerosols in this region are dominated by fine particles. In contrast, in  
 383 the central SCS, farther from the continent, AI values are smaller than AOD, suggesting that aerosols  
 384 there are primarily coarse particles from natural sources.



385  
 386 **Figure 5: Spatial distributions of MERRA-2 AOD (Jul 2002–Feb 2020) over the South China Sea, averaged**  
 387 **over different periods: (a) the southwest monsoon wet period, (b) the northeast monsoon wet period, and (c)**  
 388 **the northeast monsoon dry period. (d–f) Corresponding AI (Jul 2002–Feb 2020) averaged over the same**  
 389 **periods.**

390 Figure 6 shows the variations in macrophysical and microphysical properties of warm clouds over the  
 391 SCS during the three monsoon periods. During the SWMW period, the area-averaged warm-cloud  
 392 fraction over the SCS is the lowest ( $44.95 \pm 16.51\%$ ), whereas comparable higher values are observed  
 393 during the NEMW ( $77.21 \pm 13.23\%$ ) and NEMD ( $80.27 \pm 11.68\%$ ) periods. Although the SCS  
 394 experiences the highest water vapor content during the SWMW period, the presence of strong updrafts  
 395 enhances cloud development (Fig. 4a), leading to the lowest fraction of warm clouds and an increased  
 396 occurrence of mixed-phase and ice clouds. During the northeast monsoon, the advection of dry and cold  
 397 continental air over the SCS likely suppresses convective activity, maintaining a higher fraction of warm  
 398 clouds in the region. Additionally, During the northeast monsoon, the fraction of warm clouds is highest



删除了:

删除了: 2023

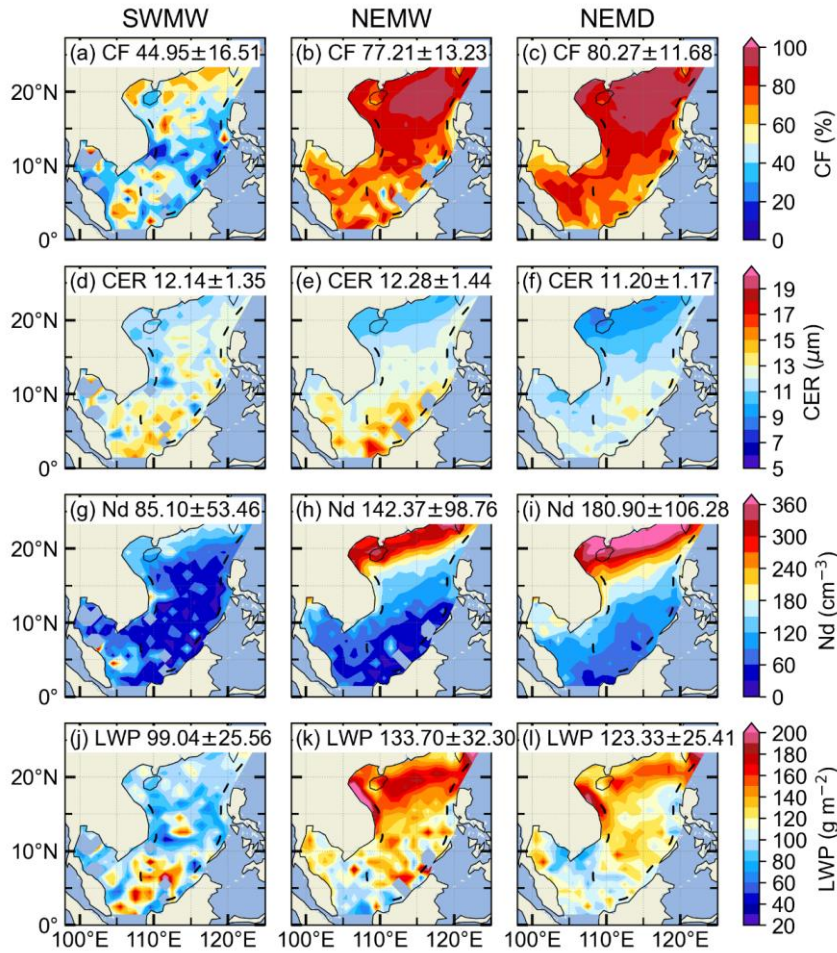
删除了: 2023

删除了:  $40.43 \pm 17.74$

删除了:  $12 \pm 14.24$

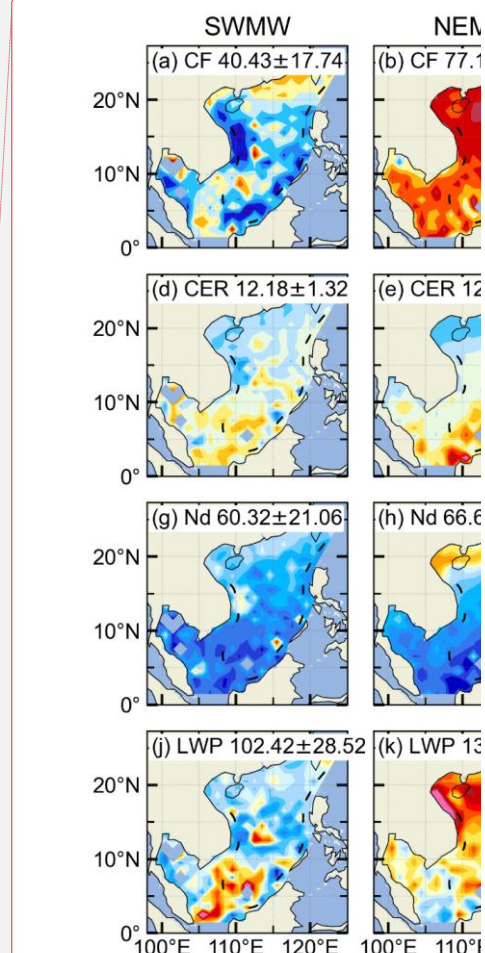
删除了:  $77.37 \pm 13.98$

405 in the northern SCS, whereas lower values are observed in the southern region near the equator, likely  
 406 due to stronger convective activity in the equatorial area.



407  
 408 **Figure 6: Spatial distributions of warm-cloud (a–c) cloud fraction, (d–f) cloud droplet effective radius, (g–i)**  
 409 **cloud droplet number concentration, and (j–l) liquid water path over the South China Sea during the**  
 410 **southwest monsoon (first column), the northeast monsoon wet period (second column), and the northeast**  
 411 **monsoon dry period (third column).**

412 The area-averaged warm-cloud droplet effective radius over the SCS is similar across the three monsoon  
 413 periods, with values of  $12.14 \pm 1.35 \mu\text{m}$  during the SWMW period,  $12.28 \pm 1.54 \mu\text{m}$  during the NEMW  
 414 period, and  $11.20 \pm 1.17 \mu\text{m}$  during the NEMD period (Figs. 6d–f). In terms of the spatial distribution of  
 415 warm-cloud droplet effective radius, droplets near the equatorial region tend to be larger than those in



删除了:

删除了: 18

删除了: 32

删除了: 41

删除了: 26

删除了: 13

422 other areas, likely due to more pronounced droplet collision and coalescence driven by precipitation,  
423 which increases droplet size.

424 The area-averaged warm-cloud droplet number concentration over the SCS exhibits distinct differences  
425 among the three periods. The lowest mean value occurs during the SWMW period ( $85.10 \pm 53.46 \text{ cm}^{-3}$ ),  
426 followed by a higher value during the NEMW period ( $142.37 \pm 98.76 \text{ cm}^{-3}$ ), and the highest value during  
427 the NEMD period ( $180.90 \pm 106.28 \text{ cm}^{-3}$ ) (Figs. 6g–i). The highest cloud droplet number concentration  
428 is observed in the northern SCS adjacent to the Chinese mainland, showing a strong spatial  
429 correspondence with aerosol distribution. Aerosol concentrations are also largest in this region (Fig. 5),  
430 consistent with the Twomey effect, whereby enhanced aerosol loading increases cloud droplet number  
431 concentration. In the southern SCS near the equator, cloud droplet number concentration is relatively  
432 low, which may be attributed to lower aerosol concentrations and/or stronger convective activity that  
433 promotes droplet growth and reduces droplet number.

434 The area-averaged warm-cloud LWP over the SCS is lowest during the SWMW period ( $99.04 \pm 25.56 \text{ g}$   
435  $\text{m}^{-2}$ ), highest during the NEMW period ( $133.70 \pm 32.30 \text{ g m}^{-2}$ ), and intermediate during the NEMD period  
436 ( $123.21 \pm 25.41 \text{ g m}^{-2}$ ) (Figs. 6j–l). During the northeast monsoon, the highest LWP values are observed  
437 in the northern SCS adjacent to the Chinese mainland. This may be attributed to more polluted  
438 environments, where the second indirect aerosol effect suppresses precipitation, thereby leading to an  
439 increase in LWP (Albrecht, 1989). It is noteworthy that the LWP in the northern SCS is higher during  
440 the NEMW period than during the NEMD period, which may be associated with sedimentation-  
441 entrainment feedback (Ackerman et al., 2004) and/or evaporation-entrainment feedbacks (Dagan et al.,  
442 2017; Wang et al., 2003). Compared with the NEMW period, the NEMD period is characterized by  
443 higher cloud droplet number concentrations and smaller CER in this region (Fig. 6e, f, h, i). These two  
444 feedbacks describe how increased droplet number concentrations and reduced droplet sizes can enhance  
445 cloud-top entrainment and evaporation, ultimately leading to a reduction in LWP (Gryspeerd et al.,  
446 2019). Additionally, under drier conditions above cloud tops during the NEMD period, the  
447 sedimentation-entrainment feedback may be further amplified, resulting in a stronger reduction in LWP  
448 (Gryspeerd et al., 2019; Sato et al., 2018). During the SWMW, LWP is also relatively high in the  
449 southern SCS near the equator (Fig. 6j). In this region, CER is larger and  $N_d$  is lower (Figs. 6d, g), likely

删除了:  $60.32 \pm 21.06$

删除了:  $66.62 \pm 29.12$

删除了:  $.23 \pm 41.71$

删除了:  $102.42 \pm 28.52$

删除了:  $134.39 \pm 31.46$

删除了: 124

删除了: 21

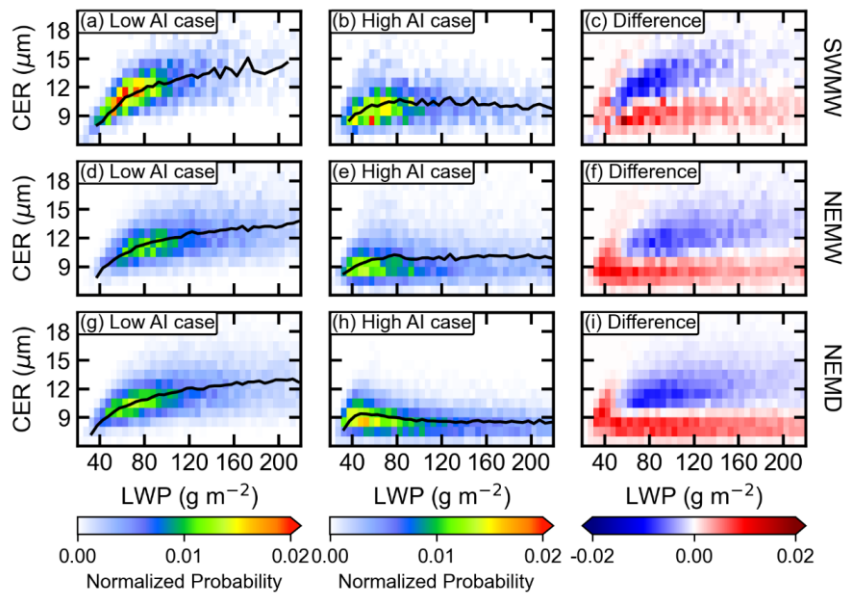
457 due to stronger updrafts near the equator, which enhance the vertical development of warm clouds and  
458 result in higher cloud water content.

459 Qualitatively, the consistency in zonal gradients of aerosol and cloud properties across all three monsoon  
460 regimes clearly reflects the theoretical ACI signal: aerosols increase  $N_d$  while reducing droplet size,  
461 which in turn lowers precipitation probability and thereby increases LWP and CF. Quantitatively,  
462 however, ACI intensities vary depending on the meteorological background (to be discussed in detail in  
463 the following section).

### 464 3.3 The Twomey Effect across the Three Periods

465 Twomey (1977) proposed that atmospheric aerosol particles can act as cloud condensation nuclei, such  
466 that an increase in aerosol loading leads to a higher cloud droplet number concentration. Under a nearly  
467 constant liquid water content, this results in smaller cloud droplet effective radius. To examine the  
468 Twomey effect during the three periods, the 25th and 75th percentiles of the AI were used to define clean  
469 ( $AI < 25$ th percentile) and polluted ( $AI > 75$ th percentile) conditions, respectively. For each condition,  
470 two-dimensional probability density distributions were calculated as a function of CER and LWP. The  
471 difference in the two-dimensional probability densities between polluted and clean conditions therefore  
472 illustrates how CER varies with aerosol loading under quasi-constant LWP. As shown in Fig. 7, CER is  
473 mostly smaller  $15\mu\text{m}$ , justifying the effectiveness of the filtering of non-raining cases. Under clean  
474 conditions, the CER of warm cloud increases with LWP across all three periods. Under polluted  
475 conditions, however, CER initially increases with LWP and then tends to level off during the SW period  
476 and the NEMW period. During the NEMD period, CER exhibits an increase followed by a decrease with  
477 increasing LWP, and subsequently remains nearly constant. The difference plots between polluted and  
478 clean conditions clearly demonstrate that polluted samples are more concentrated toward smaller CER  
479 values compared with clean samples in each quasi-constant LWP bin. This consistent shift toward  
480 smaller droplet sizes under higher aerosol loading demonstrates a clear manifestation of the Twomey  
481 effect during all three periods.

删除了: justifying

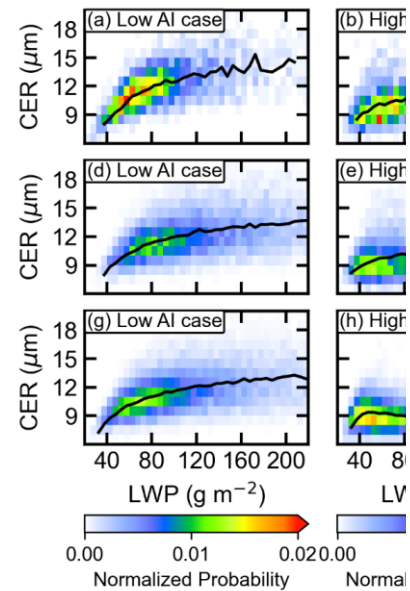


483

484 **Figure 7: Joint probability distributions of liquid water path (LWP) and cloud droplet effective radius (CER)**  
 485 **for warm clouds over the South China Sea during the three periods. The first, second, and third rows**  
 486 **correspond to the southwest monsoon, the northeast monsoon wet period, and the northeast monsoon dry**  
 487 **period, respectively. The first and second columns represent clean and polluted conditions, respectively. The**  
 488 **black lines denote the mean CER values within each LWP interval. The third column shows the differences**  
 489 **in probability density between polluted and clean conditions.**

#### 490 3.4 Variations of ACI across the Three Periods

491 As shown in Fig. 6, the warm-cloud fraction during the Southwest Monsoon Wet period is approximately  
 492 45%, while it increases to about 77% during the Northeast Monsoon Wet period and further to about 80%  
 493 during the Northeast Monsoon Dry period. This substantial difference suggests that the warm-cloud  
 494 populations sampled during different monsoon periods are fundamentally distinct and likely reflect  
 495 different cloud dynamical regimes. To better distinguish cloud morphological types within each monsoon  
 496 period and reduce potential regime-mixing effects, we further classified warm clouds over the SCS  
 497 according to CTP. Specifically, warm clouds were separated into shallow stratocumulus (CTP: 800–950  
 498 hPa) and deeper cumulus (CTP: 650–800 hPa) clouds. The ACI index were then quantified separately  
 499 for these two cloud regimes.



删除了:

501 According to the assumption of the Twomey effect (Twomey, 1977), an essential prerequisite for  
502 investigating the aerosol indirect effect based on the CER–AI relationship is to keep the LWP constant.  
503 Since CER is a function of both LWP and AI, and generally increases with LWP, variations in LWP  
504 associated with changes in aerosols can in turn modulate the CER–AI relationship. Therefore, when  
505 applying the CER–AI relationship to analyse the first aerosol indirect effect, it is essential to constrain  
506 LWP to ensure its constancy. To satisfy this requirement while maintaining sufficient sample sizes, LWP  
507 was binned at  $10 \text{ g m}^{-2}$  intervals, within which  $\text{ACI}_r$  was examined separately for shallow stratocumulus  
508 (Fig. 8a-b) and deeper cumulus clouds (Fig. 8e-f) during the three periods. The results show that for both  
509 shallow stratocumulus and deeper cumulus clouds, under both all warm-cloud conditions and non-raining  
510 warm-cloud conditions,  $\text{ACI}_r$  is generally weak when  $\text{LWP} < 50 \text{ g m}^{-2}$ , and even exhibit the anti-Twomey  
511 effect (i.e., an increase in CER with increasing aerosol loading). Clouds in this LWP regime are typically  
512 very thin or broken, as well as post-precipitation remnants (McComiskey et al., 2009). A similar  
513 phenomenon is observed over the northern Indian Ocean, which may be attributed to the intense  
514 competition for available water vapor under high aerosol concentrations, combined with the entrainment  
515 of dry air at cloud tops (Jose et al., 2020). When  $\text{LWP} > 50 \text{ g m}^{-2}$ , the  $\text{ACI}_r$  for all cloud regimes across  
516 the three periods are consistent with the Twomey effect. An exception occurs in Fig. 8b and Fig. 8d,  
517 where the  $\text{ACI}_r$  at  $\text{LWP} = 20 \text{ g m}^{-2}$  during the southwest monsoon is negative. however, this result is not  
518 statistically robust due to the limited sample size.

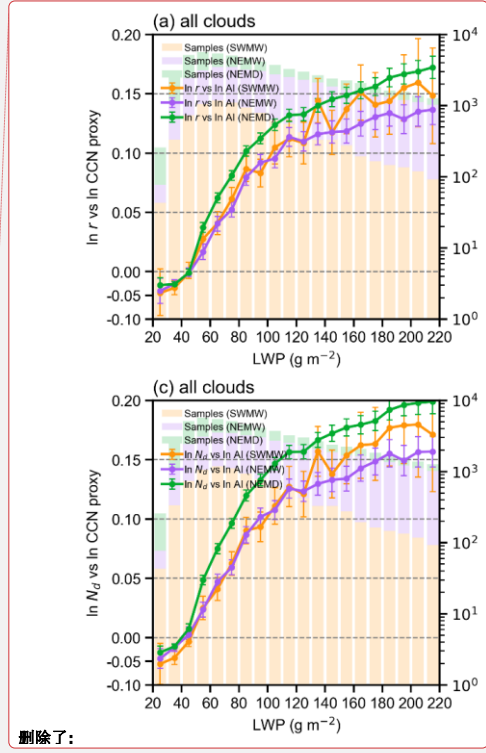
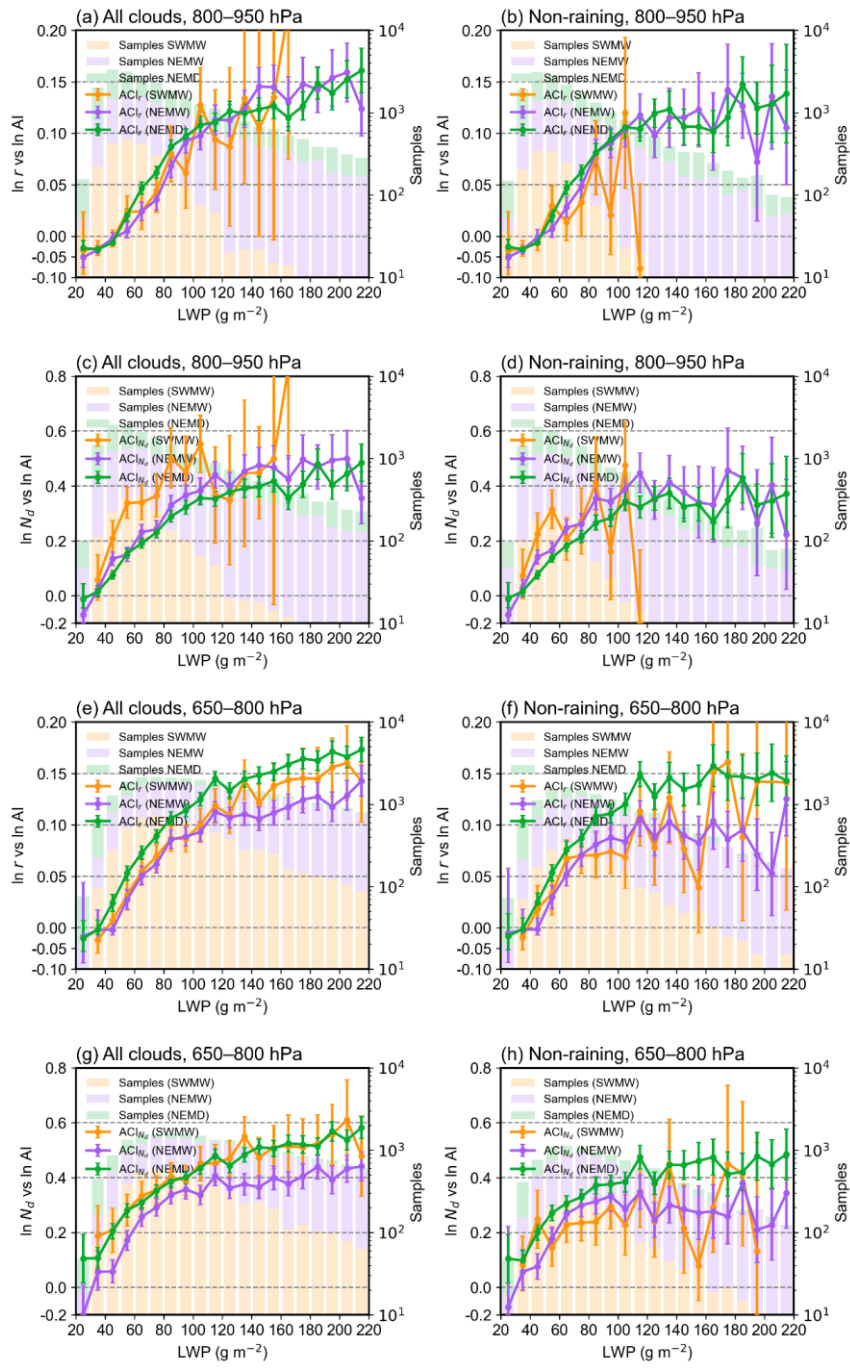
删除了: (Fig. 8a-b).

删除了: ) is observed across all three periods in the SCS when  $\text{LWP} < 50 \text{ g m}^{-2}$ .

删除了: both

删除了: warm clouds and non-raining warm clouds

删除了: 220



删除了:

527 **Figure 8: Linear regression slopes of  $\ln$  CER versus  $\ln$  AI and  $\ln$   $N_d$  versus  $\ln$  AI for shallow stratocumulus**  
528 **clouds (CTP = 800–950 hPa; a–d) and deeper cumulus clouds (CTP = 650–800 hPa; e–h) during the three**  
529 **periods. The first and second columns represent all cloud and non-raining cloud conditions, respectively.**  
530 **Green, purple, and yellow lines represent the southwest monsoon, northeast monsoon wet period, and**  
531 **northeast monsoon dry period, respectively. Error bars denote the 95 % confidence intervals of the linear**  
532 **regressions. Colored bars, consistent with the line colors, indicate the total number of samples within each**  
533 **LWP bin for the corresponding periods.**

534 Precipitation formation efficiently reduces cloud droplet number concentration and scavenges aerosols  
535 from clouds (Gryspeerd et al., 2015), introducing a sink of that does not reflect the Twomey effect (Jia et  
536 al., 2022). Therefore, when analyzing the aerosol first indirect effect in warm clouds, the influence of  
537 precipitation should be separated in order to accurately quantify the sensitivity of CER to aerosols. Fig.

538 8 shows that, for both shallow stratocumulus and deeper cumulus clouds over the SCS, the  $ACI_r$  values  
539 for all warm cloud are consistently larger than those for non-raining warm cloud across all three periods  
540 when LWP exceeds approximately  $80 \text{ g m}^{-2}$ . This indicates that the inclusion of raining samples amplifies  
541  $ACI_r$ , a phenomenon also identified in the AI/AOD– $N_d$  relationship by Jia et al. (2022) and Painemal et  
542 al. (2020). But this amplification is just an artifact governed by the joint impacts of the suppression of  
543 precipitation by aerosols and the aerosol removal by precipitation (Jia et al., 2022). Therefore, after  
544 removing precipitating clouds from all warm-cloud samples, the  $ACI_r$  obtained from non-raining warm  
545 clouds provides a more realistic representation.

546 Fig. 8b. shows that, under non-raining warm-cloud conditions with  $LWP > 50 \text{ g m}^{-2}$ , the period-to-period  
547 variations in  $ACI_r$  differ between shallow stratocumulus and deeper cumulus clouds over the SCS. For  
548 shallow stratocumulus  $ACI_r$  values are broadly comparable across the three periods, with no significant  
549 differences (Fig. 8b). In contrast, deeper cumulus clouds exhibit clear differences among the three periods,  
550 (Fig. 8f), with  $ACI_r$  generally strongest during the NEMD period, while the NEMW and SWMW periods  
551 show comparatively weaker values, with the NEMW period exceeding the SWMW period in some LWP  
552 bins. For  $LWP > 140 \text{ g m}^{-2}$ , the  $ACI_r$  during the southwest monsoon exhibits large fluctuations due to  
553 the limited number of samples, even exceeding that of the northeast monsoon. The analysis in Section  
554 3.2 reveals substantial differences in atmospheric conditions over the SCS among the three periods.  
555 During the SWMW period, atmospheric moisture and sea surface temperatures reach their highest levels,  
556 and upward motion dominates over the region, while aerosol concentrations remain relatively low.

删除了: (a, b)

删除了: (c, d)

删除了: all warm

删除了: , c

删除了: non-raining warm

删除了: b, d

删除了: in

删除了: clouds

删除了: clouds

删除了:  $ACI_r$

删除了: differs

删除了: , being largest

删除了: followed by

删除了: period, and smallest during the southwest monsoon. For

删除了:  $> 160$

572 During the NEMW period, moisture and sea surface temperatures are still relatively high, with upward  
573 motion primarily confined to the southern areas near the equator, and aerosol concentrations are elevated  
574 due to pollution transported from continental China. In contrast, during the NEMD period, atmospheric  
575 moisture and sea surface temperatures are at their lowest, subsidence dominates, and aerosol  
576 concentrations reach their maximum. These results suggest that although the large-scale environmental  
577 statistics differ substantially among the three monsoon periods, the local thermodynamic conditions  
578 favourable for shallow stratocumulus formation may be relatively similar across periods. Such cloud-  
579 favourable environments may not be fully resolved by the period-mean large-scale statistics presented  
580 here, which could explain the broadly comparable  $ACI_r$  values for shallow stratocumulus. In contrast,  
581  $ACI_r$  for deeper cumulus clouds over the SCS generally tends to strengthen under drier and more stable  
582 monsoon environments, with the strongest signals occurring during the NEMD period, while no  
583 consistent ordering is observed between the NEMW and SWMW periods across different LWP bins.  
584 Accordingly, the subsequent analysis focuses on the period-to-period differences of deeper cumulus  
585 clouds  $ACI$  and its relationship with variations in the monsoon environmental background.

586 In addition to the radius-based  $ACI_r$ , we further examined the droplet-number susceptibility ( $ACI_{Nd}$ )  
587 separately for shallow stratocumulus (Fig. 8c–d) and deeper cumulus clouds (Fig. 8g–h). Consistent with  
588 the  $ACI_r$  results,  $ACI_{Nd}$  for shallow stratocumulus remains broadly comparable across the three monsoon  
589 periods, with no significant differences. Deeper cumulus clouds exhibit clear period-to-period variations,  
590 with the strongest signals occurring during the NEMD period, while comparatively weaker values are  
591 observed during the SWMW and NEMW periods. Such consistency highlights that the observed period-  
592 to-period differences in  $ACI$  are governed by systematic changes in the underlying meteorological  
593 environment rather than by the choice of  $ACI$  metric. Motivated by this consistency, Section 3.5  
594 investigates how variations in moisture and LTS regulate the evolution of deeper cumulus clouds  $ACI$   
595 across the three periods.

### 596 3.5 Causes of $ACI$ Variations across the Three Periods

597 The progressive enhancement of  $ACI_r$  and  $ACI_{Nd}$  for deeper cumulus clouds from the SWMW to the  
598 NEMD period (Fig. 8) may potentially be influenced by the aerosol hygroscopic swelling artifact. The  
599 MERRA-2 AOD used to construct AI is calculated under ambient RH, with the extinction coefficients

删除了: Under these distinct atmospheric conditions, warm-cloud  $ACI$  over the SCS weaken progressively from the NEMW period to the NEMD period and further to the southwest monsoon.

删除了: .

删除了: .

删除了: also increases progressively from the SWMW to the NEMW and further to the NEMD period, indicating that the strengthening of  $ACI_r$ ...

删除了: is robust across both microphysical metrics

609 of sulfate, hydrophilic carbonaceous aerosols, and sea salt explicitly parameterized as functions of RH  
 610 (Randles et al., 2017). Under humid conditions, aerosol hygroscopic growth can increase AOD, and  
 611 therefore AI, without a corresponding increase in CCN-active particle number. This may artificially  
 612 flatten the CER–AI and Nd–AI regression slopes, leading to apparently weaker ACI under moister  
 613 conditions. Given that the SWMW and NEMW periods are characterized by substantially higher  
 614 moisture levels than the NEMD period, the weaker ACI observed during these moister periods could  
 615 partly reflect this hygroscopic swelling artifact rather than intrinsic differences in cloud microphysical  
 616 sensitivity.

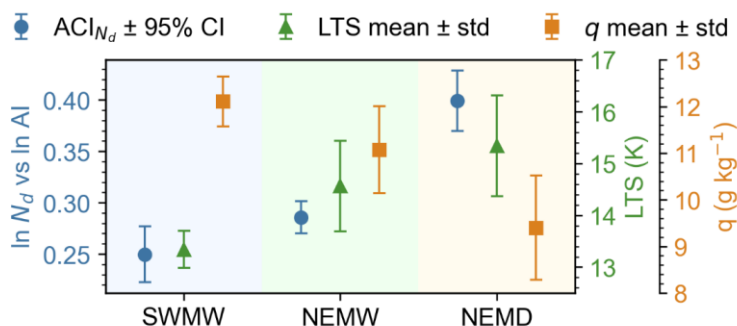
617 To assess whether the observed period-to-period differences are substantially affected by systematic  
 618 humidity differences, we further stratified the data from each monsoon period into three RH ranges (0–  
 619 45 %, 45–80 %, and 80–100 %). Under constrained LWP (50–200 g m<sup>-2</sup>) and cloud-top pressure (650–  
 620 800 hPa) conditions, ACI<sub>Nd</sub> was recalculated separately for each subsample. As shown in Table 2, all RH  
 621 bins consistently exhibit the same enhancement pattern from SWMW to NEMW and further to NEMD.  
 622 These results suggest that although AI may be affected by hygroscopic swelling under humid  
 623 environments, this effect is insufficient to explain the systematic ACI differences among the three  
 624 monsoon periods. Therefore, aerosol hygroscopic swelling is unlikely to be the dominant cause of the  
 625 observed period-to-period variability, motivating further examination of the thermodynamic and  
 626 moisture controls on ACI.

627 **Table 2: ACI<sub>Nd</sub> ± 95%CI of deeper cumulus clouds under different relative humidity bins during the three**  
 628 **periods.**

Period	RH<45%	45% ≤ RH < 80%	80% ≤ RH ≤ 100%
SWMW	-0.126 ± 0.291	0.221 ± 0.043	0.278 ± 0.038
NEMW	-0.055 ± 0.194	0.262 ± 0.032	0.312 ± 0.018
NEMD	0.127 ± 0.102	0.371 ± 0.022	0.377 ± 0.012

629 To provide an integrated view of how the ACI of deeper cumulus clouds co-varies with the  
 630 thermodynamic and moisture background across the three periods, Fig. 9 shows the ACI<sub>Nd</sub> together with  
 631 the corresponding q and LST. Both ACI<sub>Nd</sub> and the key environmental regulators display a coherent  
 632 evolution across the three periods. From the SWMW to the NEMW and NEMD, ACI<sub>Nd</sub> intensify steadily,

633 in parallel with declining moisture and increasing LTS. Quantitatively, The  $ACI_{N_d}$  increases  
 634 progressively from  $0.250 \pm 0.027$  (95% confidence interval, 95% CI) during the SWMW period to  $0.286$   
 635  $\pm 0.016$  during NEMW and further to  $0.399 \pm 0.029$  during NEMD. Meanwhile,  $q$  decreases from  $12.111$   
 636  $\pm 0.540 \text{ g kg}^{-1}$  during SWMW to  $11.072 \pm 0.931 \text{ g kg}^{-1}$  during NEMW and  $9.540 \pm 1.120 \text{ g kg}^{-1}$  during  
 637 NEMD, while the LTS increases from  $13.341 \pm 0.358 \text{ K}$  to  $14.565 \pm 0.875 \text{ K}$  and  $15.343 \pm 0.977 \text{ K}$ ,  
 638 respectively. (All  $q$  and LTS uncertainties represent one standard deviation, std.) These co-varying  
 639 changes indicate that both  $q$  and LTS may regulate the strengthening of ACI across the three periods  
 640 over the SCS. In the following subsections, we separately examine the roles of  $q$  (Section 3.5.1) and LTS  
 641 (Section 3.5.2) in regulating ACI.

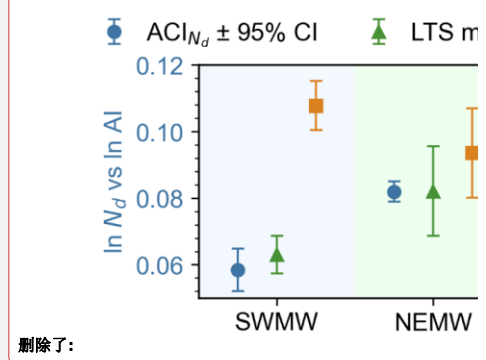


642  
 643 **Figure 9:**  $ACI_{N_d}$ , specific humidity ( $q$ ), and lower-tropospheric stability (LTS) for the three periods over the  
 644 South China Sea. The 95% confidence interval (CI) represents the uncertainty derived from the Student's  $t$   
 645 test, whereas std denotes the one standard deviation.

### 646 3.5.1 Water vapor

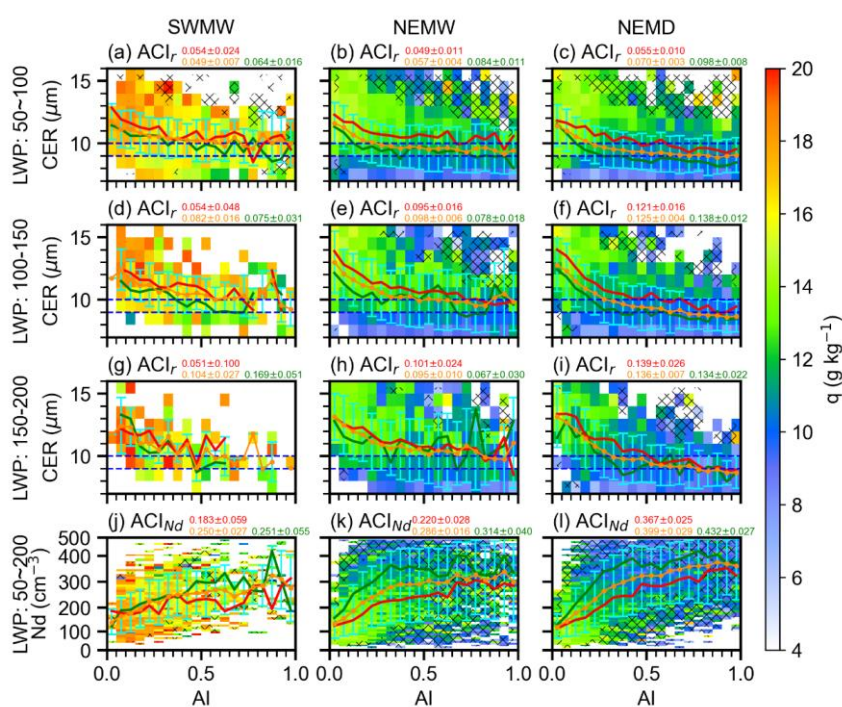
647 Water vapor supply substantially impacts CCN activation, droplet condensational growth, and  
 648 coalescence, hence altering the cloud droplet size distribution (Feingold et al., 2006; Zheng et al., 2022).  
 649 Specific humidity at 1000 hPa serves as a proxy for the ambient water vapor available to warm clouds,  
 650 analogous to the use of near-surface specific humidity as a proxy for marine boundary layer moisture in  
 651 previous studies (Dadashazar et al., 2020). To investigate the influence of water vapor on ACI in deeper  
 652 cumulus clouds, specific humidity was averaged within each AI-CER/ $N_d$  interval separately for each  
 653 period (Fig. 10). For each AI interval, CER/ $N_d$  was further averaged, and samples were stratified by the  
 654 25th and 75th percentiles of specific humidity to represent dry ( $< 25$ th percentile) and moist ( $> 75$ th

- 删除了: 058
- 删除了: 006
- 删除了: 082
- 删除了: 003
- 删除了: 108
- 删除了: 002
- 删除了: 126
- 删除了: 526
- 删除了: 113
- 删除了: 961
- 删除了: 500
- 删除了: 100
- 删除了: 338
- 删除了: 361
- 删除了: 566
- 删除了: 862
- 删除了: 349
- 删除了: 980

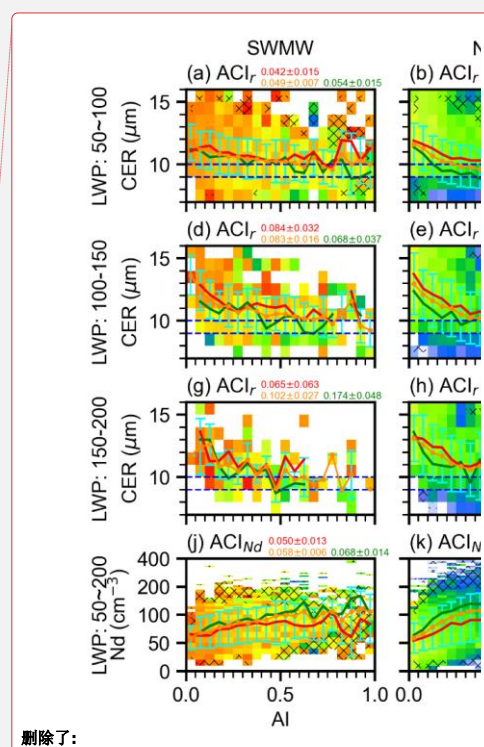


删除了:

674 percentile) conditions, under which the corresponding mean CER/ $N_d$  was calculated. In addition, ACI  
 675 was derived from all samples and separately for the dry and moist subsets in each period. To satisfy the  
 676 LWP constraint required for the CER–AI analysis, the influence of water vapor on ACI was examined  
 677 within LWP intervals of 50–100, 100–150, and 150–200  $\text{g m}^{-2}$ . In addition, because the  $N_d$ –AI  
 678 relationship does not require an explicit LWP constraint for  $ACI_{N_d}$  calculation, it was examined over the  
 679 broader LWP range of 50–200  $\text{g m}^{-2}$ .



680  
 681 **Figure 10: Influence of water vapor on ACI in deeper cumulus clouds (CTP: 650-800 hPa) across the three**  
 682 **periods. Rows 1–3 show mean specific humidity in CER–AI bins for LWP ranges of 50–100, 100–150, and**  
 683 **150–200  $\text{g m}^{-2}$ , respectively; row 4 shows mean specific humidity in  $N_d$ –AI bins for LWP 50–200  $\text{g m}^{-2}$ .**  
 684 **Columns correspond to the southwest monsoon, northeast monsoon wet period, and northeast monsoon dry**  
 685 **period. Yellow dashed, red, and green lines denote the mean CER (rows 1–3) or  $N_d$  (row 4) in each AI bin for**  
 686 **all samples, for moist conditions (specific humidity > 75th percentile), and for dry conditions (specific**  
 687 **humidity < 25th percentile), respectively. Error bars indicate the standard deviation of CER (rows 1–3) or**  
 688  **$N_d$  (row 4) within each AI bin. Yellow numbers indicate  $ACI \pm 95\%$  uncertainty estimates (according to a**  
 689 **Student’s t test) for all samples, whereas red and green numbers indicate the corresponding estimates under**  
 690 **moist and dry conditions, respectively.**



删除了:

692 As shown in Fig. 10, higher specific humidity conditions are generally associated with larger CER and  
693 lower  $N_d$  across the three periods over the SCS. This may suggest that abundant water vapor enhances  
694 condensational growth of cloud droplets, and the enlarged droplets are more susceptible to collision-  
695 coalescence, which not only reduces  $N_d$  but also further increases the CER. By contrast, under limited  
696 water vapor availability, the ability of CCN-activated droplets to grow by condensation is substantially  
697 constrained. The lack of a sufficient number of larger droplets favors condensation as the predominant  
698 growth mechanism, thereby yielding smaller droplet sizes (Zheng et al., 2022).

699 The response of ACI to environmental water availability exhibits different behaviors. Qiu et al. (2017)  
700 analysed the AI-CER relationship for non-raining warm clouds over the Southern Great Plains and found  
701 the anti-Twomey effect under moist conditions. Zheng et al. (2022) investigated non-raining warm  
702 clouds over the Eastern North Atlantic and found that sufficient water vapor availability can enhance  
703 ACI. Over the SCS, within the LWP range of 50–200  $\text{g m}^{-2}$ ,  $\text{ACI}_{N_d}$  is consistently smaller under moist  
704 conditions than under dry conditions across all three periods (Figs. 10j–l), suggesting that  $N_d$  exhibits  
705 weaker sensitivity to aerosol perturbations in moist environments compared to dry environments. Figs.  
706 10j–l show that  $N_d$  exhibits comparable values between moist and dry conditions at very low aerosol  
707 loading. As aerosol concentration increases, however,  $N_d$  becomes smaller under moist conditions  
708 relative to dry conditions. This pattern may indicate that under ample water vapor availability, increased  
709 aerosol loading initially enhances cloud droplet activation, leading to elevated droplet number  
710 concentrations. But subsequent collision-coalescence promotes droplet growth while reducing  $N_d$ .  
711 Consequently, the microphysical adjustments associated with enhanced moisture availability dampen the  
712 sensitivities of  $N_d$  to aerosol perturbations, manifesting as weaker  $\text{ACI}_{N_d}$  in the moist regime.

713 In contrast, the response of  $\text{ACI}_r$  to moisture exhibits a dependence on LWP. At low LWP (50–100  $\text{g m}^{-2}$ ),  
714  $\text{ACI}_r$  is reduced under moist relative to dry conditions across all periods (Figs. 10a–c). At higher LWP  
715 ranges, this reduction appears only in the Southwest Monsoon period within the 100–150  $\text{g m}^{-2}$  and 150–  
716 200  $\text{g m}^{-2}$  bins, and in the Northeast Monsoon Dry period within the 100–150  $\text{g m}^{-2}$  bin (Fig. 10g), while  
717 the opposite response is observed in other cases. The LWP is defined as the column-integrated liquid  
718 water content within clouds (e.g., existing cloud droplets) (Lee and Penner, 2011). At low LWP,  $\text{ACI}_r$  is  
719 weaker under moist conditions (as indicated by 1000-hPa specific humidity) compared to dry conditions

删除了:  $^{-2}$  range

删除了: whereas

删除了: holds for the

723 (Figs. 10a–c). A possible explanation is that in moist environments, enhanced collision-coalescence  
724 processes promote droplet growth, leading to larger CER. In contrast, under drier conditions, limited  
725 water vapor availability inhibits droplet growth, resulting in smaller CER. At higher LWP, when the in-  
726 cloud liquid water content is abundant, the response of  $ACI_r$  to environmental water vapor variations  
727 becomes less consistent (Figs. 10d–i), suggesting the involvement of additional microphysical or  
728 dynamical processes.

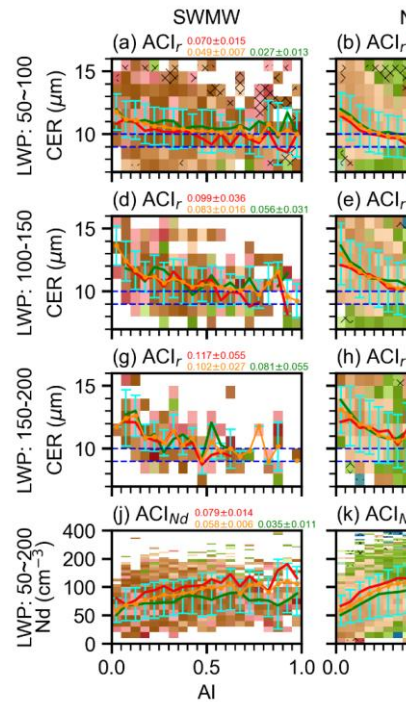
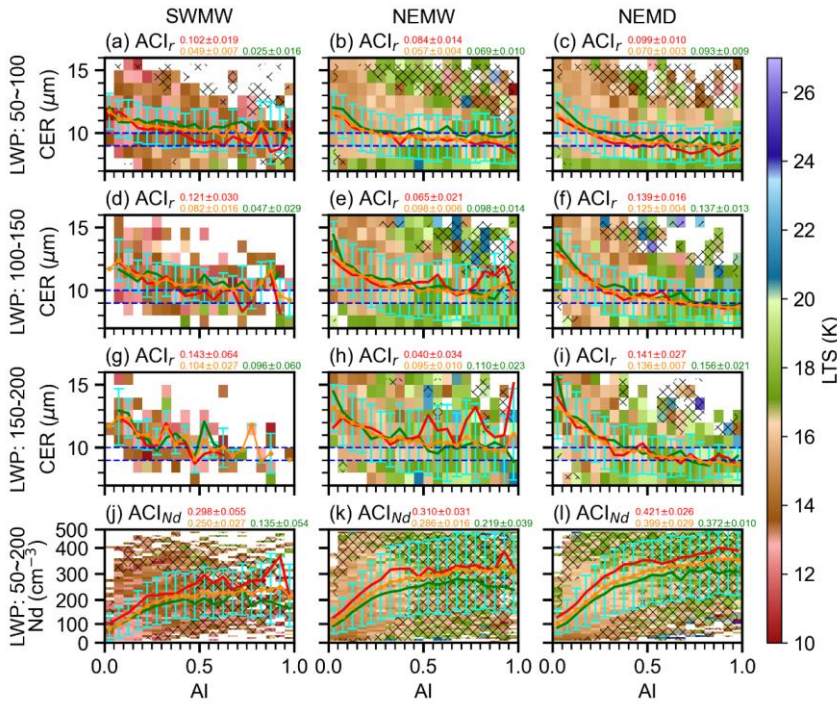
729 Over the SCS, CER and  $N_d$  exhibit comparable values across the three periods within the same LWP  
730 interval at low AI. As AI increases, noticeable differences develop, with CER decreasing progressively  
731 from the SW to the NEMW and further to the NEMD, while  $N_d$  increases accordingly (Fig. 10).  
732 Consequently, ACI is enhanced stepwise from SW to NEMW and then to NEMD. This stepwise  
733 enhancement may be partly attributed to the progressive decrease in environmental water vapor from  
734 SW to NEMW and further to NEMD (Figs. 4a–c), particularly evident within the LWP interval of 50–  
735 100  $g\ m^{-2}$ .

### 736 3.5.2 lower tropospheric stability

737 Thermodynamic and dynamic conditions are key factors influencing aerosol vertical transport, aerosol  
738 activation processes, and cloud droplet formation. Thermodynamic stability can be quantitatively  
739 represented by the lower tropospheric stability (LTS), a measure of temperature inversion strength  
740 initially defined for marine stratocumulus clouds (Klein and Hartmann, 1993). This metric has been  
741 widely utilized to evaluate atmospheric stability and vertical mixing across both oceanic and continental  
742 regions (Jia et al., 2019; Ma et al., 2018b). Higher LTS values represent enhanced lower tropospheric  
743 stability, which suppresses vertical mixing and convective initiation. To further examine the influence of  
744 thermodynamic conditions on ACI [in deeper cumulus clouds](#), the LTS was analysed in a manner identical  
745 to that used for specific humidity. For each period, samples were stratified by the 25th and 75th  
746 percentiles of LTS to represent unstable and stable conditions, respectively, and ACI was computed for  
747 each subset (Fig. 11). The analysis was performed within LWP intervals of 50–100, 100–150, and 150–  
748 200  $g\ m^{-2}$  for the CER–AI relationship, and over 50–200  $g\ m^{-2}$  for the  $N_d$ -AI relationship. Fig. 11 shows  
749 that stronger lower tropospheric stability (higher LTS) is associated with smaller CER and higher  $N_d$ , as

750 enhanced static stability may suppresses convective mixing and vertical moisture transport, thereby  
 751 limiting droplet growth while favouring higher droplet concentrations.

删除了: favoring



删除了:

752  
 753 **Figure 11: Same as Fig. 10, but for lower tropospheric stability. Stable and unstable conditions correspond to**  
 754 **the upper (> 75th percentile) and lower (< 25th percentile) quartiles of LTS, respectively. Yellow numbers**  
 755 **indicate  $ACI \pm 95\%$  uncertainty estimates (according to a Student's t test) for all samples, whereas red and**  
 756 **green numbers indicate the corresponding estimates under stable and unstable conditions, respectively.**

757 In contrast to unstable conditions, stronger  $ACI_{Nd}$  is observed under stable conditions characterized by  
 758 higher LTS values (Figs. 11j-l). This result suggests that enhanced LTS may facilitate aerosol  
 759 accumulation and coagulation, leading to an increase in aerosol particle size. Larger particles are more  
 760 efficient on acting as CCN, thereby promoting cloud droplet activation and formation. The suppressed  
 761 vertical mixing associated with stable stratification may further confine aerosols and moisture within the  
 762 boundary layer, strengthening local ACI. Consequently, the sensitivity of Nd to aerosol perturbations is  
 763 enhanced under stable conditions, manifesting as higher  $ACI_{Nd}$  relative to unstable environments. Over  
 764 the SCS, LTS is generally weaker during the southwest monsoon than during the northeast monsoon (Fig.

767 11). The stronger atmospheric stability associated with the northeast monsoon favors enhanced ACI in  
768 warm clouds, resulting in stronger ACI during the NE compared with the SW.

769 The response of ACI<sub>r</sub> to LTS exhibits distinct behaviours across different LWP intervals and periods  
770 (Figs. 11a–i). During the southwest monsoon period, ACI<sub>r</sub> is consistently larger under stable conditions  
771 than under unstable conditions across all three LWP ranges, consistent with the ACI<sub>Nd</sub> results. However,  
772 during the northeast monsoon wet period, this enhancement is only evident in the lowest LWP range  
773 (50–100 g m<sup>-2</sup>). In the northeast monsoon dry period, the enhancement under stable conditions is  
774 observed in both the 50–100 g m<sup>-2</sup> and 100–150 g m<sup>-2</sup> bins. This contrasting behaviour (Figs. 11e, h, i)  
775 can be further understood from the AI-CER relationships. At low AI values, corresponding to relatively  
776 clean conditions, CER is larger under unstable conditions than under stable conditions. As AI increases,  
777 indicating more polluted environments, CER under stable and unstable conditions gradually converges,  
778 leading to stronger ACI<sub>r</sub> under unstable conditions. This pattern may indicate that during the northeast  
779 monsoon period, when in-cloud water vapor is abundant and aerosol loading is relatively high, cloud  
780 microphysical processes become less sensitive to variations in LTS. The inherently strong and weakly  
781 variable lower-tropospheric stability during the northeast monsoon may suppress the dynamical  
782 influence of further LTS changes ACI, thereby weakening the LTS dependence of ACI<sub>r</sub> under moist and  
783 polluted conditions.

#### 784 4 discussion and conclusions

785 To investigate how ACI vary under the alternating influence of two opposing monsoon systems over the  
786 South China Sea (SCS) and how different environmental conditions modulate these interactions, the  
787 study period was divided into three representative phases based on variations in wind direction,  
788 precipitation, and specific humidity: the southwest monsoon (SW), the northeast monsoon wet period  
789 (NEMW), and the northeast monsoon dry period (NEMD). By integrating reanalysis data and satellite  
790 observations, this study examined the variations in ACI and the associated environmental controlling  
791 factors during these three periods. The main findings are summarized as follows:

792 1. SCS exhibits distinct seasonal environmental conditions associated with the prevailing monsoon  
793 regimes. During the SW, the SCS is dominated by strong upward motion, high SSTs, and abundant

删除了: behaviors

删除了: NEMW and NEMD periods, such an

删除了: within

删除了: interval

删除了: At higher LWP ranges (100-150 and 150-200 g m<sup>-2</sup>), ACI<sub>r</sub> becomes smaller

删除了: relative to unstable ones.

删除了: behavior

删除了: , f

删除了: moist

804 atmospheric moisture. During the NEMW, continental outflow transports aerosols over the SCS while  
805 SSTs decrease and LTS strengthens; ascent is largely confined to the equatorial south and moisture  
806 remains relatively high. During the NEMD, continental influence persists but the environment becomes  
807 drier and more stable, with the lowest SSTs and widespread subsidence, favouing the boundary-layer  
808 accumulation of fine-mode aerosols. These contrasting meteorological and environmental conditions  
809 among the SW, NEMW, and NEMD periods establish a distinct seasonal background over the SCS and  
810 exert a decisive influence on ACI.

删除了: favoring

811 2. A pronounced Twomey effect was consistently identified across all three periods, as indicated by  
812 smaller CER and higher Nd with increasing aerosol loading under nearly constant LWP. Quantitative  
813 estimates of ACI, show that the Twomey effect dominates when LWP exceeds  $50 \text{ g m}^{-2}$ , whereas an  
814 apparent “anti-Twomey” behaviour appears in optically thin clouds ( $\text{LWP} < 50 \text{ g m}^{-2}$ ), likely associated  
815 with strong competition for limited water vapor and entrainment-induced drying. Precipitation tends to  
816 amplify the ACI by simultaneously suppressing cloud droplet number concentrations and removing  
817 aerosols from the atmosphere. After removing raining samples, the ACI derived from non-raining warm  
818 clouds provides a more reliable representation of the first aerosol indirect effect, reducing biases caused  
819 by precipitation processes. Across the three periods, shallow stratocumulus clouds (CTP: 800–950 hPa)  
820 show limited variability in ACI, while deeper cumulus clouds (CTP: 650–800 hPa) exhibit a clear  
821 increase from SWMW to NEMW, and further to NEMD, reaching a maximum in NEMD.

删除了: behavior

删除了: Among

删除了: is smallest during the SW, increases during the

删除了: ,

删除了: reaches its

删除了: during the

删除了: plays

822 3. Environmental conditions exert a strong influence on deeper cumulus cloud ACI intensity over the  
823 SCS. Water vapor availability may play a critical role in regulating cloud droplet activation and growth.

824  $\text{ACI}_{\text{Nd}}$  is consistently smaller under moist conditions than under dry conditions across all three periods,  
825 indicating that Nd exhibits weaker sensitivity to aerosol perturbations in moist environments compared

826 to dry environments. Thermodynamic stability may also modulate ACI variability.  $\text{ACI}_{\text{Nd}}$  is generally  
827 enhanced under stable atmospheric conditions, as stronger LTS may suppress vertical mixing and confine

删除了: modulates

828 aerosols and moisture within the boundary layer, thereby facilitating aerosol accumulation and  
829 potentially promoting CCN activation. Overall, deeper cumulus cloud ACI tends to be more pronounced

删除了: is most

830 in dry and stable environments, which are typical of the NEMD, and weakest under moist and  
831 convectively active environments during the SWMW. However, these conclusions should be treated with

删除了: SW

843 caution, as the present analysis cannot fully disentangle the respective influences of water vapor,  
844 thermodynamic stability, cloud regime, and aerosol type and loading. These factors co-vary  
845 systematically with the monsoon phase, which limits attribution of the observed inter-period ACI  
846 differences to any single controlling mechanism.

847 It is worth noting that the use of AI as a CCN proxy may be affected by aerosol hygroscopic swelling,  
848 introducing additional uncertainty in the period-to-period variations of deeper cumulus cloud ACI.  
849 However, a consistent increasing tendency across the three periods is still observed within all relative  
850 humidity bins, indicating that the inter-period differences are not primarily driven by hygroscopic  
851 swelling effects, but are more likely controlled by systematic changes in the environmental conditions.

852 In addition, the coexistence of sea-salt coarse-mode and anthropogenic fine-mode aerosols over the South  
853 China Sea introduces uncertainty in using AI as a CCN proxy, particularly due to its limited  
854 representation of giant CCN associated with sea salt. This may weaken the diagnosed Twomey effect  
855 and introduce additional uncertainty in ACI estimates. Future work will focus on explicitly separating  
856 aerosol types to better quantify their respective roles in cloud microphysical processes during different  
857 monsoon periods.

858 Furthermore, the Nd retrieval assumes a constant sub-adiabatic factor ( $f_{ad} = 0.8$ ), which may introduce  
859 a systematic offset in Nd estimation (Gryspeerd et al., 2022). Such an assumption may vary in validity  
860 under different meteorological conditions and could potentially introduce seasonal biases, thereby  
861 affecting the magnitude of the derived ACI and the inter-period ACI gradient.

862 Overall, deeper cumulus cloud ACI increases from SW to NEMW and further to NEMD, consistent with  
863 co-varying decreases in moisture and increases in atmospheric stability. However, the simultaneous  
864 variation of moisture, stability, cloud regime, and aerosol loading across monsoon phases limits the  
865 attribution of their individual contributions to the observed inter-period differences. These results  
866 highlight that the coupling among aerosols, moisture, and thermodynamic stability exerts fundamental  
867 control over marine warm-cloud microphysical processes in tropical monsoon regions. The findings  
868 provide important observational evidence for understanding ACI and offer valuable guidance for  
869 improving the representation of ACI in climate and numerical weather prediction models.

870

删除了: Overall,  
删除了: strength

删除了: SCS

删除了: progressively  
删除了: the  
删除了: primarily driven by decreasing  
删除了: availability  
删除了: increasing

879 Financial support

880 This work was supported by the National Natural Science Foundation of China (grant nos. 42027804,  
881 41775026, and 41075012). Hailing Jia was support by the project ACIaction (File No.  
882 OCENW.M.24.024) financed by the Dutch Research Council (NWO) under the grant  
883 <https://doi.org/10.61686/OZRJI30024>.

884

885 Acknowledgements

886 Data and samples were collected onboard of R/V Shiyan 6 implementing the open research cruise  
887 NORC2024-07 supported by NSFC Shiptime Sharing Project (project number: 42349907). And we  
888 sincerely appreciate the valuable comments provided by the two anonymous reviewers, which  
889 significantly enhanced the clarity and robustness of this work.

890

891 Competing Interest

892 The authors declare that they have no known competing financial interests or personal relationships that  
893 could have appeared to influence the work reported in this paper.

894

895 Author contributions

896 YL analysed the data and wrote the manuscript. HJ participated in scientific discussions and reviewed  
897 and refined the manuscript. YH participated in scientific discussions, and Resources, Project  
898 administration, Funding acquisition, Conceptualization, Formal analysis, Methodology, Writing –  
899 review & editing.

900

901 Data Availability

902 Atmospheric fields were obtained from the ERA5 reanalysis datasets produced by the European Centre  
903 for Medium-Range Weather Forecasts (ECMWF) via the Copernicus Climate Change Service (C3S)  
904 Climate Data Store (CDS). The data are publicly available at <https://cds.climate.copernicus.eu/>.

905 Aerosol datasets were obtained from the Modern-Era Retrospective Analysis for Research and  
906 Applications Version 2 (MERRA-2), produced by the NASA Goddard Earth Observing System (GEOS)

删除了: HJ and

删除了: and reviewed and refined the manuscript

909 Global Modeling and Assimilation Office (GMAO) and distributed by the Goddard Earth Sciences Data  
910 and Information Services Center (GES DISC). The data are publicly available at  
911 <https://disc.gsfc.nasa.gov/datasets?project=MERRA-2>.  
912 Cloud retrievals were obtained from the Clouds and the Earth's Radiant Energy System (CERES)-  
913 Moderate Resolution Imaging Spectroradiometer (MODIS) Edition 4 Single Scanner Footprint (SSF)  
914 daily Level-3 products ( $1^\circ \times 1^\circ$  grid), produced by NASA's Langley Research Center (LaRC) and  
915 distributed by the Atmospheric Science Data Center (ASDC). The CERES–MODIS data are publicly  
916 available through the NASA ASDC archive at <https://ceres.larc.nasa.gov/data/#ssf1deg-level-3>.  
917 Sea surface temperature (SST) data were obtained from the National Oceanic and Atmospheric  
918 Administration (NOAA) Optimum Interpolation (OI) SST, Version 2, produced by the NOAA Physical  
919 Sciences Laboratory. The data are publicly available through the NOAA Physical Sciences Laboratory  
920 at <https://psl.noaa.gov/data/gridded/data.noaa.oisst.v2.html>.  
921 IMERG V07 precipitation data used in this study are openly available from the NASA Goddard Earth  
922 Sciences Data and Information Services Center (GES DISC) at  
923 <https://disc.gsfc.nasa.gov/datasets?keywords=gpm%20imerg%2007>, as cited in Huffman et al. (2024).  
924

## 925 **References**

926 Ackerman, A. S., Kirkpatrick, M. P., Stevens, D. E., and Toon, O. B.: The impact of humidity above  
927 stratiform clouds on indirect aerosol climate forcing, *Nature*, 432, 1014–1017,  
928 <https://doi.org/10.1038/nature03174>, 2004.  
929 Albrecht, B. A.: Aerosols, Cloud Microphysics, and Fractional Cloudiness, *Science*, 245, 1227–1230,  
930 1989.  
931 Bellouin, N., Quaas, J., Gryspeerdt, E., Kinne, S., Stier, P., Watson-Parris, D., Boucher, O., Carslaw, K.  
932 S., Christensen, M., Daniau, A.-L., Dufresne, J.-L., Feingold, G., Fiedler, S., Forster, P., Gettelman, A.,  
933 Haywood, J. M., Lohmann, U., Malavelle, F., Mauritsen, T., McCoy, D. T., Myhre, G., Mühlenthal, J.,  
934 Neubauer, D., Possner, A., Rugenstein, M., Sato, Y., Schulz, M., Schwartz, S. E., Sourdeval, O.,  
935 Storelvmo, T., Toll, V., Winker, D., and Stevens, B.: Bounding Global Aerosol Radiative Forcing of  
936 Climate Change, *Reviews of Geophysics*, 58, e2019RG000660, <https://doi.org/10.1029/2019RG000660>,  
937 2020.

938 [Chen, J. and Hu, Z.:](#) Seasonal variability in spatial patterns of sea surface cold- and warm fronts over the  
939 continental shelf of the northern South China Sea, *Front. Mar. Sci.*, 9,  
940 <https://doi.org/10.3389/fmars.2022.1100772>, 2023.

941 Chen, Y., Luo, T., Sun, G., Zhu, W., Liu, Q., Liu, Y., Jin, X., and Weng, N.: A Comprehensive Ensemble  
942 Model for Marine Atmospheric Boundary-Layer Prediction in Meteorologically Sparse and Complex  
943 Regions: A Case Study in the South China Sea, *Remote Sensing*, 17, 2046,  
944 <https://doi.org/10.3390/rs17122046>, 2025.

945 Chen, Y.-C., Christensen, M. W., Stephens, G. L., and Seinfeld, J. H.: Satellite-based estimate of global  
946 aerosol–cloud radiative forcing by marine warm clouds, *Nature Geosci*, 7, 643–646,  
947 <https://doi.org/10.1038/ngeo2214>, 2014.

948 Costantino, L. and Bréon, F.-M.: Aerosol indirect effect on warm clouds over South-East Atlantic, from  
949 co-located MODIS and CALIPSO observations, *Atmospheric Chemistry and Physics*, 13, 69–88,  
950 <https://doi.org/10.5194/acp-13-69-2013>, 2013.

951 Dadashazar, H., Crosbie, E., Majdi, M. S., Panahi, M., Moghaddam, M. A., Behrang, A., Brunke, M.,  
952 Zeng, X., Jonsson, H. H., and Sorooshian, A.: Stratocumulus cloud clearings: statistics from satellites,  
953 reanalysis models, and airborne measurements, *Atmos Chem Phys*, 20, 4637–4665,  
954 <https://doi.org/10.5194/acp-20-4637-2020>, 2020.

955 [Dagan, G., Koren, I., Altaratz, O., and Heiblum, R. H.:](#) Time-dependent, non-monotonic response of  
956 warm convective cloud fields to changes in aerosol loading, *Atmospheric Chemistry and Physics*, 17,  
957 7435–7444, <https://doi.org/10.5194/acp-17-7435-2017>, 2017.

958 Dezfuli, A. K., Ichoku, C. M., Huffman, G. J., Mohr, K. I., Selker, J. S., Van De Giesen, N., Hochreutener,  
959 R., and Annor, F. O.: Validation of IMERG Precipitation in Africa, *Journal of Hydrometeorology*, 18,  
960 2817–2825, <https://doi.org/10.1175/JHM-D-17-0139.1>, 2017.

961 Douglas, A. and L’Ecuyer, T.: Quantifying variations in shortwave aerosol–cloud–radiation interactions  
962 using local meteorology and cloud state constraints, *Atmospheric Chemistry and Physics*, 19, 6251–6268,  
963 <https://doi.org/10.5194/acp-19-6251-2019>, 2019.

964 Douville, H., Raghavan, K., Renwick, J., Allan, R. P., Arias, P. A., Barlow, M., Cerezo-Mota, R., Cherchi,  
965 A., Gan, T. Y., and Gergis, J.: *Climate Change 2021 – The Physical Science Basis: Working Group I*  
966 *Contribution to the Sixth Assessment Report of the Intergovernmental Panel on Climate Change*, 1st ed.,  
967 Cambridge University Press, <https://doi.org/10.1017/9781009157896>, 2023.

968 Durden, S. L.: Evaluation of IMERG Data over Open Ocean Using Observations of Tropical Cyclones,  
969 *Remote Sensing*, 16, 2028, <https://doi.org/10.3390/rs16112028>, 2024.

970 Fan, J., Yuan, T., Comstock, J. M., Ghan, S., Khain, A., Leung, L. R., Li, Z., Martins, V. J., and  
971 Ovchinnikov, M.: Dominant role by vertical wind shear in regulating aerosol effects on deep convective

删除了: Braun, R. A., Dadashazar, H., MacDonald, A. B., Crosbie, E., Jonsson, H. H., Woods, R. K., Flagan, R. C., Seinfeld, J. H., and Sorooshian, A.: Cloud Adiabaticity and Its Relationship to Marine Stratocumulus Characteristics Over the Northeast Pacific Ocean, *Journal of Geophysical Research: Atmospheres*, 123, 13,790–13,806, <https://doi.org/10.1029/2018JD029287>, 2018.

删除了: Dadashazar, H., Painemal, D., Alipanah, M., Brunke, M., Chellappan, S., Corral, A. F., Crosbie, E., Kirschler, S., Liu, H., Moore, R. H., Robinson, C., Scarino, A. J., Shook, M., Sinclair, K., Thornhill, K. L., Voigt, C., Wang, H., Winstead, E., Zeng, X., Ziemba, L., Zuidema, P., and Sorooshian, A.: Cloud drop number concentrations over the western North Atlantic Ocean: seasonal cycle, aerosol interrelationships, and other influential factors, *Atmos. Chem. Phys.*, 21, 10499–10526, <https://doi.org/10.5194/acp-21-10499-2021>, 2021.

987 clouds, *Journal of Geophysical Research: Atmospheres*, 114, <https://doi.org/10.1029/2009JD012352>,  
988 2009.

989 Fan, J., Wang, Y., Rosenfeld, D., and Liu, X.: Review of Aerosol–Cloud Interactions: Mechanisms,  
990 Significance, and Challenges, <https://doi.org/10.1175/JAS-D-16-0037.1>, 2016.

991 Feingold, G., Remer, L. A., Ramaprasad, J., and Kaufman, Y. J.: Analysis of smoke impact on clouds in  
992 Brazilian biomass burning regions: An extension of Twomey’s approach, *J. Geophys. Res.*, 106, 22907–  
993 22922, <https://doi.org/10.1029/2001JD000732>, 2001.

994 Feingold, G., Furrer, R., Pilewskie, P., Remer, L. A., Min, Q., and Jonsson, H.: Aerosol indirect effect  
995 studies at Southern Great Plains during the May 2003 Intensive Operations Period, *Journal of*  
996 *Geophysical Research: Atmospheres*, 111, <https://doi.org/10.1029/2004JD005648>, 2006.

997 Gelaro, R., McCarty, W., Suárez, M. J., Todling, R., Molod, A., Takacs, L., Randles, C. A., Darmenov,  
998 A., Bosilovich, M. G., Reichle, R., Wargan, K., Coy, L., Cullather, R., Draper, C., Akella, S., Buchard,  
999 V., Conaty, A., Silva, A. M. da, Gu, W., Kim, G.-K., Koster, R., Lucchesi, R., Merkova, D., Nielsen, J.  
1000 E., Partyka, G., Pawson, S., Putman, W., Rienecker, M., Schubert, S. D., Sienkiewicz, M., and Zhao, B.:  
1001 The Modern-Era Retrospective Analysis for Research and Applications, Version 2 (MERRA-2),  
1002 <https://doi.org/10.1175/JCLI-D-16-0758.1>, 2017.

1003 Grosvenor, D. P., Sourdeval, O., Zuidema, P., Ackerman, A., Alexandrov, M. D., Bennartz, R., Boers,  
1004 R., Cairns, B., Chiu, J. C., Christensen, M., Deneke, H., Diamond, M., Feingold, G., Fridlind, A.,  
1005 Hünerbein, A., Knist, C., Kollias, P., Marshak, A., McCoy, D., Merk, D., Painemal, D., Rausch, J.,  
1006 Rosenfeld, D., Russchenberg, H., Seifert, P., Sinclair, K., Stier, P., van Diedenhoven, B., Wendisch, M.,  
1007 Werner, F., Wood, R., Zhang, Z., and Quaas, J.: Remote Sensing of Droplet Number Concentration in  
1008 Warm Clouds: A Review of the Current State of Knowledge and Perspectives, *Reviews of Geophysics*,  
1009 56, 409–453, <https://doi.org/10.1029/2017RG000593>, 2018.

1010 Gryspeerdt, E., Stier, P., White, B. A., and Kipling, Z.: Wet scavenging limits the detection of aerosol  
1011 effects on precipitation, *Atmospheric Chemistry and Physics*, 15, 7557–7570,  
1012 <https://doi.org/10.5194/acp-15-7557-2015>, 2015.

1013 Gryspeerdt, E., Goren, T., Sourdeval, O., Quaas, J., Mülmenstädt, J., Dipu, S., Unglaub, C., Gettelman,  
1014 A., and Christensen, M.: Constraining the aerosol influence on cloud liquid water path, *Atmospheric*  
1015 *Chemistry and Physics*, 19, 5331–5347, <https://doi.org/10.5194/acp-19-5331-2019>, 2019.

1016 [Gryspeerdt, E., McCoy, D. T., Crosbie, E., Moore, R. H., Nott, G. J., Painemal, D., Small-Griswold, J.,](https://doi.org/10.5194/amt-15-3875-2022)  
1017 [Sorooshian, A., and Ziemba, L.: The impact of sampling strategy on the cloud droplet number](https://doi.org/10.5194/amt-15-3875-2022)  
1018 [concentration estimated from satellite data, \*Atmospheric Measurement Techniques\*, 15, 3875–3892,](https://doi.org/10.5194/amt-15-3875-2022)  
1019 <https://doi.org/10.5194/amt-15-3875-2022>, 2022.

1020 Hayden, L. J. M., Tan, J., Bolvin, D. T., and Huffman, G. J.: Variations in the Diurnal Cycle of  
1021 Precipitation and Its Changes with Distance from Shore over Two Contrasting Regions as Observed by

1022 IMERG, ERA5, and Spaceborne Ku Radar, *Journal of Hydrometeorology*, 24, 675–689,  
1023 <https://doi.org/10.1175/JHM-D-22-0154.1>, 2023.

1024 Hersbach, H., Bell, B., Berrisford, P., Hirahara, S., Horányi, A., Muñoz-Sabater, J., Nicolas, J., Peubey,  
1025 C., Radu, R., Schepers, D., Simmons, A., Soci, C., Abdalla, S., Abellan, X., Balsamo, G., Bechtold, P.,  
1026 Biavati, G., Bidlot, J., Bonavita, M., De Chiara, G., Dahlgren, P., Dee, D., Diamantakis, M., Dragani, R.,  
1027 Flemming, J., Forbes, R., Fuentes, M., Geer, A., Haimberger, L., Healy, S., Hogan, R. J., Hólm, E.,  
1028 Janisková, M., Keeley, S., Laloyaux, P., Lopez, P., Lupu, C., Radnoti, G., De Rosnay, P., Rozum, I.,  
1029 Vamborg, F., Villaume, S., and Thépaut, J.: The ERA5 global reanalysis, *Quart J Royal Meteor Soc*,  
1030 146, 1999–2049, <https://doi.org/10.1002/qj.3803>, 2020.

1031 Huffman, G. J., Bolvin, D. T., Braithwaite, D., Hsu, K.-L., Joyce, R. J., Kidd, C., Nelkin, E. J.,  
1032 Sorooshian, S., Stocker, E. F., Tan, J., Wolff, D. B., and Xie, P.: Integrated Multi-satellite Retrievals for  
1033 the Global Precipitation Measurement (GPM) Mission (IMERG), in: *Satellite Precipitation Measurement*,  
1034 vol. 67, edited by: Levizzani, V., Kidd, C., Kirschbaum, D. B., Kummerow, C. D., Nakamura, K., and  
1035 Turk, F. J., Springer International Publishing, Cham, 343–353, [https://doi.org/10.1007/978-3-030-24568-9\\_19](https://doi.org/10.1007/978-3-030-24568-9_19), 2020.

1037 Huffman, G. J., Bolvin, D. T., Braithwaite, D., Hsu, K., Joyce, R., Kidd, C., Nelkin, E., Sorooshian, S.,  
1038 Tan, J., and Xie, P.: NASA Global Precipitation Measurement (GPM) Integrated Multi-Satellite  
1039 Retrievals for GPM (IMERG) Version 07, Algorithm Theoretical Basis Document (ATBD) Version, 47,  
1040 2023.

1041 Jia, H. and Quaas, J.: Nonlinearity of the cloud response postpones climate penalty of mitigating air  
1042 pollution in polluted regions, *Nat. Clim. Chang.*, 13, 943–950, <https://doi.org/10.1038/s41558-023-01775-5>, 2023.

1044 Jia, H., Ma, X., Quaas, J., Yin, Y., and Qiu, T.: Is positive correlation between cloud droplet effective  
1045 radius and aerosol optical depth over land due to retrieval artifacts or real physical processes?, *Atmos.*  
1046 *Chem. Phys.*, 19, 8879–8896, <https://doi.org/10.5194/acp-19-8879-2019>, 2019.

1047 Jia, H., Ma, X., Yu, F., and Quaas, J.: Significant underestimation of radiative forcing by aerosol–cloud  
1048 interactions derived from satellite-based methods, *Nat Commun*, 12, 3649,  
1049 <https://doi.org/10.1038/s41467-021-23888-1>, 2021.

1050 Jia, H., Quaas, J., Gryspeerd, E., Böhm, C., and Sourdeval, O.: Addressing the difficulties in quantifying  
1051 droplet number response to aerosol from satellite observations, *Atmospheric Chemistry and Physics*, 22,  
1052 7353–7372, <https://doi.org/10.5194/acp-22-7353-2022>, 2022.

1053 [Jia, H., Hasekamp, O., and Quaas, J.: Revisiting Aerosol–Cloud Interactions From Weekly Cycles,](https://doi.org/10.1029/2024gl1108266)  
1054 [Geophysical Research Letters](https://doi.org/10.1029/2024gl1108266), 51, <https://doi.org/10.1029/2024gl1108266>, 2024.

1055 Jose, S., Nair, V. S., and Babu, S. S.: Anthropogenic emissions from South Asia reverses the aerosol  
1056 indirect effect over the northern Indian Ocean, *Sci Rep*, 10, 18360, <https://doi.org/10.1038/s41598-020-74897-x>, 2020.

1058 Kim, B.-G., Schwartz, S. E., Miller, M. A., and Min, Q.: Effective radius of cloud droplets by ground-  
1059 based remote sensing: Relationship to aerosol, *Journal of Geophysical Research: Atmospheres*, 108,  
1060 <https://doi.org/10.1029/2003JD003721>, 2003.

1061 Klein, S. A. and Hartmann, D. L.: *The Seasonal Cycle of Low Stratiform Clouds*, 1993.

1062 Lee, S. S. and Penner, J. E.: Dependence of aerosol–cloud interactions in stratocumulus clouds on liquid-  
1063 water path, *Atmospheric Environment*, 45, 6337–6346, <https://doi.org/10.1016/j.atmosenv.2011.08.050>,  
1064 2011.

1065 Lee, T.-W. and Park, J. E.: Thermodynamic correlations between the sea surface temperature, water  
1066 vapor content, and cloud fraction, using MODIS data, *Theor Appl Climatol*, 150, 1699–1706,  
1067 <https://doi.org/10.1007/s00704-022-04261-8>, 2022.

1068 Liu, J., Yu, J., Lin, C., He, M., Liu, H., Wang, W., and Min, M.: Near-real-time atmospheric and oceanic  
1069 science products of Himawari-8 and Himawari-9 geostationary satellites over the South China Sea, *Earth  
1070 System Science Data*, 16, 4949–4969, <https://doi.org/10.5194/essd-16-4949-2024>, 2024.

1071 Ma, P.-L., Rasch, P. J., Chepfer, H., Winker, D. M., and Ghan, S. J.: Observational constraint on cloud  
1072 susceptibility weakened by aerosol retrieval limitations, *Nat Commun*, 9, 2640,  
1073 <https://doi.org/10.1038/s41467-018-05028-4>, 2018a.

1074 Ma, X., Jia, H., Yu, F., and Quaas, J.: Opposite Aerosol Index-Cloud Droplet Effective Radius  
1075 Correlations Over Major Industrial Regions and Their Adjacent Oceans, *Geophysical Research Letters*,  
1076 45, 5771–5778, <https://doi.org/10.1029/2018GL077562>, 2018b.

1077 Martin, D. W. and Howland, M. R.: Rainfall over the Arabian Sea during the onset of the 1979 monsoon,  
1078 *Nature*, 300, 628–630, <https://doi.org/10.1038/300628a0>, 1982.

1079 ~~McComiskey, A., Feingold, G., Frisch, A. S., Turner, D. D., Miller, M. A., Chiu, J. C., Min, Q., and~~  
1080 ~~Ogren, J. A.: An assessment of aerosol-cloud interactions in marine stratus clouds based on surface~~  
1081 ~~remote sensing, *J. Geophys. Res.*, 114, 2008JD011006, <https://doi.org/10.1029/2008JD011006>, 2009.~~

1082 Miller, R. M., Rauber, R. M., Di Girolamo, L., Rilloraza, M., Fu, D., McFarquhar, G. M., Nesbitt, S. W.,  
1083 Ziemba, L. D., Woods, S., and Thornhill, K. L.: Influence of natural and anthropogenic aerosols on cloud  
1084 base droplet size distributions in clouds over the South China Sea and West Pacific, *Atmospheric  
1085 Chemistry and Physics*, 23, 8959–8977, <https://doi.org/10.5194/acp-23-8959-2023>, 2023.

1086 Minnis, P., Sun-Mack, S., Young, D. F., Heck, P. W., Garber, D. P., Chen, Y., Spangenberg, D. A.,  
1087 Arduini, R. F., Trepte, Q. Z., Smith, W. L., Ayers, J. K., Gibson, S. C., Miller, W. F., Hong, G.,  
1088 Chakrapani, V., Takano, Y., Liou, K.-N., Xie, Y., and Yang, P.: CERES Edition-2 Cloud Property  
1089 Retrievals Using TRMM VIRS and Terra and Aqua MODIS Data—Part I: Algorithms, *IEEE  
1090 Transactions on Geoscience and Remote Sensing*, 49, 4374–4400,  
1091 <https://doi.org/10.1109/TGRS.2011.2144601>, 2011a.

删除了: Martin, G. M., Johnson, D. W., and Spice, A.: The  
Measurement and Parameterization of Effective Radius of Droplets in  
Warm Stratocumulus Clouds, 1994.

1095 Minnis, P., Sun-Mack, S., Chen, Y., Khaiyer, M. M., Yi, Y., Ayers, J. K., Brown, R. R., Dong, X., Gibson,  
 1096 S. C., Heck, P. W., Lin, B., Nordeen, M. L., Nguyen, L., Palikonda, R., Smith, W. L., Spangenberg, D.  
 1097 A., Trepte, Q. Z., and Xi, B.: CERES Edition-2 Cloud Property Retrievals Using TRMM VIRS and Terra  
 1098 and Aqua MODIS Data—Part II: Examples of Average Results and Comparisons With Other Data, *IEEE*  
 1099 *Transactions on Geoscience and Remote Sensing*, 49, 4401–4430,  
 1100 <https://doi.org/10.1109/TGRS.2011.2144602>, 2011b.

1101 Minnis, P., Sun-Mack, S., Chen, Y., Chang, F.-L., Yost, C. R., Smith, W. L., Heck, P. W., Arduini, R.  
 1102 F., Bedka, S. T., Yi, Y., Hong, G., Jin, Z., Painemal, D., Palikonda, R., Scarino, B. R., Spangenberg, D.  
 1103 A., Smith, R. A., Trepte, Q. Z., Yang, P., and Xie, Y.: CERES MODIS Cloud Product Retrievals for  
 1104 Edition 4—Part I: Algorithm Changes, *IEEE Transactions on Geoscience and Remote Sensing*, 59,  
 1105 2744–2780, <https://doi.org/10.1109/TGRS.2020.3008866>, 2021.

1106 Nakajima, T., Higurashi, A., Kawamoto, K., and Penner, J. E.: A possible correlation between satellite-  
 1107 derived cloud and aerosol microphysical parameters, *Geophysical Research Letters*, 28, 1171–1174,  
 1108 <https://doi.org/10.1029/2000GL012186>, 2001.

1109 Ou, H., Cai, M., Zhang, Y., Ni, X., Liang, B., Sun, Q., Mai, S., Sun, C., Zhou, S., Wang, H., Sun, J., and  
 1110 Zhao, J.: Measurement report: Cloud condensation nuclei (CCN) activity in the South China Sea from  
 1111 shipborne observations during the summer and winter of 2021 – seasonal variation and anthropogenic  
 1112 influence, *Atmospheric Chemistry and Physics*, 25, 2495–2513, [https://doi.org/10.5194/acp-25-2495-](https://doi.org/10.5194/acp-25-2495-2025)  
 1113 2025, 2025.

1114 Painemal, D.: Global estimates of changes in shortwave low-cloud albedo and fluxes due to variations  
 1115 in cloud droplet number concentration derived from CERES-MODIS satellite sensors, *Geophys Res Lett*,  
 1116 45, 9288–9296, <https://doi.org/10.1029/2018GL078880>, 2018.

1117 Painemal, D., Chang, F.-L., Ferrare, R., Burton, S., Li, Z., Smith Jr., W. L., Minnis, P., Feng, Y., and  
 1118 Clayton, M.: Reducing uncertainties in satellite estimates of aerosol–cloud interactions over the  
 1119 subtropical ocean by integrating vertically resolved aerosol observations, *Atmospheric Chemistry and*  
 1120 *Physics*, 20, 7167–7177, <https://doi.org/10.5194/acp-20-7167-2020>, 2020.

1121 Peng, S., Zhu, Y., Huang, K., Ding, X., Shi, R., Wu, D., Feng, Y., and Wang, D.: Detecting the structure  
 1122 of marine atmospheric boundary layer over the Northern South China Sea by shipboard GPS sondes,  
 1123 *Atmospheric Science Letters*, 17, 564–568, <https://doi.org/10.1002/asl.693>, 2016.

1124 Qiu, Y., Zhao, C., Guo, J., and Li, J.: 8-Year ground-based observational analysis about the seasonal  
 1125 variation of the aerosol-cloud droplet effective radius relationship at SGP site, *Atmospheric Environment*,  
 1126 164, 139–146, <https://doi.org/10.1016/j.atmosenv.2017.06.002>, 2017.

1127 [Randles, C. A., Silva, A. M. da, Buchar, V., Colarco, P. R., Darmenov, A., Govindaraju, R., Smirnov,](https://doi.org/10.1175/JCLI-D-16-0609.1)  
 1128 [A., Holben, B., Ferrare, R., Hair, J., Shinozuka, Y., and Flynn, C. J.: The MERRA-2 Aerosol Reanalysis,](https://doi.org/10.1175/JCLI-D-16-0609.1)  
 1129 [1980 Onward. Part I: System Description and Data Assimilation Evaluation,](https://doi.org/10.1175/JCLI-D-16-0609.1)  
 1130 <https://doi.org/10.1175/JCLI-D-16-0609.1>, 2017.

删除了: Painemal, D., Corral, A. F., Sorooshian, A., Brunke, M. A.,  
 Chellappan, S., Afzali Gorooh, V., Ham, S.-H., O'Neill, L., Smith Jr.,  
 W. L., Tselioudis, G., Wang, H., Zeng, X., and Zuidema, P.: An  
 Overview of Atmospheric Features Over the Western North Atlantic  
 Ocean and North American East Coast—Part 2: Circulation,  
 Boundary Layer, and Clouds, *Journal of Geophysical Research:*  
*Atmospheres*, 126, e2020JD033423,  
<https://doi.org/10.1029/2020JD033423>, 2021.

- 1139 Reynolds, R. W., Rayner, N. A., Smith, T. M., Stokes, D. C., and Wang, W.: An Improved In Situ and  
1140 Satellite SST Analysis for Climate, 2002.
- 1141 Rosenfeld, D., Zhu, Y., Wang, M., Zheng, Y., Goren, T., and Yu, S.: Aerosol-driven droplet  
1142 concentrations dominate coverage and water of oceanic low-level clouds, *Science*, 363, eaav0566,  
1143 <https://doi.org/10.1126/science.aav0566>, 2019.
- 1144 Saponaro, G., Kolmonen, P., Sogacheva, L., Rodriguez, E., Virtanen, T., and De Leeuw, G.: Estimates  
1145 of the aerosol indirect effect over the Baltic Sea region derived from 12 years of MODIS observations,  
1146 *Atmos. Chem. Phys.*, 17, 3133–3143, <https://doi.org/10.5194/acp-17-3133-2017>, 2017.
- 1147 Sato, Y., Goto, D., Michibata, T., Suzuki, K., Takemura, T., Tomita, H., and Nakajima, T.: Aerosol  
1148 effects on cloud water amounts were successfully simulated by a global cloud-system resolving model,  
1149 *Nat Commun*, 9, 985, <https://doi.org/10.1038/s41467-018-03379-6>, 2018.
- 1150 Seinfeld, J. H., Bretherton, C., Carslaw, K. S., Coe, H., DeMott, P. J., Dunlea, E. J., Feingold, G., Ghan,  
1151 S., Guenther, A. B., Kahn, R., Kraucunas, I., Kreidenweis, S. M., Molina, M. J., Nenes, A., Penner, J. E.,  
1152 Prather, K. A., Ramanathan, V., Ramaswamy, V., Rasch, P. J., Ravishankara, A. R., Rosenfeld, D.,  
1153 Stephens, G., and Wood, R.: Improving our fundamental understanding of the role of aerosol–cloud  
1154 interactions in the climate system, *Proceedings of the National Academy of Sciences*, 113, 5781–5790,  
1155 <https://doi.org/10.1073/pnas.1514043113>, 2016.
- 1156 Sorooshian, A., Anderson, B., Bauer, S. E., Braun, R. A., Cairns, B., Crosbie, E., Dadashazar, H., Diskin,  
1157 G., Ferrare, R., Flagan, R. C., Hair, J., Hostetler, C., Jonsson, H. H., Kleb, M. M., Liu, H., MacDonald,  
1158 A. B., McComiskey, A., Moore, R., Painemal, D., Russell, L. M., Seinfeld, J. H., Shook, M., Smith, W.  
1159 L., Thornhill, K., Tselioudis, G., Wang, H., Zeng, X., Zhang, B., Ziemba, L., and Zuidema, P.: Aerosol–  
1160 Cloud–Meteorology Interaction Airborne Field Investigations: Using Lessons Learned from the U.S.  
1161 West Coast in the Design of ACTIVATE off the U.S. East Coast, <https://doi.org/10.1175/BAMS-D-18-0100.1>, 2019.
- 1163 Stier, P., Van Den Heever, S. C., Christensen, M. W., Gryspeerdt, E., Dagan, G., Saleeby, S. M.,  
1164 Bollasina, M., Donner, L., Emanuel, K., Ekman, A. M. L., Feingold, G., Field, P., Forster, P., Haywood,  
1165 J., Kahn, R., Koren, I., Kummerow, C., L'Ecuyer, T., Lohmann, U., Ming, Y., Myhre, G., Quaas, J.,  
1166 Rosenfeld, D., Samset, B., Seifert, A., Stephens, G., and Tao, W.-K.: Multifaceted aerosol effects on  
1167 precipitation, *Nat. Geosci.*, 17, 719–732, <https://doi.org/10.1038/s41561-024-01482-6>, 2024.
- 1168 Su, W., Loeb, N. G., Xu, K.-M., Schuster, G. L., and Eitzen, Z. A.: An estimate of aerosol indirect effect  
1169 from satellite measurements with concurrent meteorological analysis, *Journal of Geophysical Research:*  
1170 *Atmospheres*, 115, <https://doi.org/10.1029/2010JD013948>, 2010.
- 1171 Sun, Q., Liang, B., Cai, M., Zhang, Y., Ou, H., Ni, X., Sun, X., Han, B., Deng, X., Zhou, S., and Zhao,  
1172 J.: Cruise observation of the marine atmosphere and ship emissions in South China Sea: Aerosol  
1173 composition, sources, and the aging process, *Environmental Pollution*, 316, 120539,  
1174 <https://doi.org/10.1016/j.envpol.2022.120539>, 2023.

- 1175 Tan, J., Huffman, G. J., Bolvin, D. T., and Nelkin, E. J.: Diurnal Cycle of IMERG V06 Precipitation,  
1176 Geophysical Research Letters, 46, 13584–13592, <https://doi.org/10.1029/2019GL085395>, 2019a.
- 1177 Tan, J., Huffman, G. J., Bolvin, D. T., and Nelkin, E. J.: IMERG V06: Changes to the Morphing  
1178 Algorithm, <https://doi.org/10.1175/JTECH-D-19-0114.1>, 2019b.
- 1179 Tu, Q., Zhao, Y., Guo, J., Cheng, C., Shi, L., Yan, Y., and Hao, Z.: Spatial and Temporal Variations of  
1180 Aerosol Optical Thickness over the China Seas from Himawari-8, Remote Sensing, 13, 5082,  
1181 <https://doi.org/10.3390/rs13245082>, 2021.
- 1182 Twomey, S.: Pollution and the planetary albedo, Atmospheric Environment (1967), 8, 1251–1256,  
1183 [https://doi.org/10.1016/0004-6981\(74\)90004-3](https://doi.org/10.1016/0004-6981(74)90004-3), 1974.
- 1184 Twomey, S.: The Influence of Pollution on the Shortwave Albedo of Clouds, 1977.
- 1185 Wall, C. J., Norris, J. R., Possner, A., McCoy, D. T., McCoy, I. L., and Lutsko, N. J.: Assessing effective  
1186 radiative forcing from aerosol–cloud interactions over the global ocean, Proceedings of the National  
1187 Academy of Sciences, 119, e2210481119, <https://doi.org/10.1073/pnas.2210481119>, 2022.
- 1188 [Wall, C. J., Storelvmo, T., and Possner, A.: Global observations of aerosol indirect effects from marine](https://doi.org/10.5194/acp-23-13125-2023)  
1189 [liquid clouds. Atmospheric Chemistry and Physics, 23, 13125–13141, https://doi.org/10.5194/acp-23-](https://doi.org/10.5194/acp-23-13125-2023)  
1190 [13125-2023, 2023.](https://doi.org/10.5194/acp-23-13125-2023)
- 1191 Wang, B., LinHo, Zhang, Y., and Lu, M.-M.: Definition of South China Sea Monsoon Onset and  
1192 Commencement of the East Asia Summer Monsoon, <https://doi.org/10.1175/2932.1>, 2004.
- 1193 Wang, B., Huang, F., Wu, Z., Yang, J., Fu, X., and Kikuchi, K.: Multi-scale climate variability of the  
1194 South China Sea monsoon: A review, Dynamics of Atmospheres and Oceans, 47, 15–37,  
1195 <https://doi.org/10.1016/j.dynatmoce.2008.09.004>, 2009.
- 1196 Wang, F., Guo, J., Wu, Y., Zhang, X., Deng, M., Li, X., Zhang, J., and Zhao, J.: Satellite observed  
1197 aerosol-induced variability in warm cloud properties under different meteorological conditions over  
1198 eastern China, Atmospheric Environment, 84, 122–132, <https://doi.org/10.1016/j.atmosenv.2013.11.018>,  
1199 2014.
- 1200 Wang, J.-J., Li, X., and Carey, L. D.: Evolution, Structure, Cloud Microphysical, and Surface Rainfall  
1201 Processes of Monsoon Convection during the South China Sea Monsoon Experiment, Journal of the  
1202 Atmospheric Sciences, 64, 360–380, <https://doi.org/10.1175/JAS3852.1>, 2007.
- 1203 Wang K.-Y., Sui C.-H., Lu M.-M., and Hong J.-S.: Cold Surge Impacts on the Structure, Energy Budget,  
1204 and Turbulence of the South China Sea Boundary Layer, <https://doi.org/10.1175/MWR-D-23-0238.1>,  
1205 2024a.
- 1206 Wang, S., Wang, Q., and Feingold, G.: Turbulence, Condensation, and Liquid Water Transport in  
1207 Numerically Simulated Nonprecipitating Stratocumulus Clouds, 2003.

1208 Wang, Y., Zhao, P., Xiao, H., and Zhang, P.: Aerosol effects on liquid cloud microphysical properties in  
1209 south China: Land–ocean contrasts, *Atmospheric Pollution Research*, 15, 102032,  
1210 <https://doi.org/10.1016/j.apr.2023.102032>, 2024b.

1211 Wang, Y., Li, J., Fang, F., Zhang, P., He, J., Pöhlker, M. L., Henning, S., Tang, C., Jia, H., Wang, Y.,  
1212 Jian, B., Shi, J., and Huang, J.: In-situ observations reveal weak hygroscopicity in the Southern Tibetan  
1213 Plateau: implications for aerosol activation and indirect effects, *npj Clim Atmos Sci*, 7, 77,  
1214 <https://doi.org/10.1038/s41612-024-00629-x>, 2024c.

1215 Wang, Y., Jia, H., Zhang, P., Fang, F., Li, J., Zhu, L., Wang, Y., Wang, T., and Li, J.: Sensitivity of cloud  
1216 microphysics to aerosol is highly associated with cloud water content: Implications for indirect radiative  
1217 forcing, *Atmospheric Research*, 309, 107552, <https://doi.org/10.1016/j.atmosres.2024.107552>, 2024d.

1218 Watters, D. and Battaglia, A.: The Summertime Diurnal Cycle of Precipitation Derived from IMERG,  
1219 *Remote Sensing*, 11, 1781, <https://doi.org/10.3390/rs11151781>, 2019.

1220 Watters, D., Battaglia, A., and Allan, R. P.: The Diurnal Cycle of Precipitation according to Multiple  
1221 Decades of Global Satellite Observations, Three CMIP6 Models, and the ECMWF Reanalysis, *Journal*  
1222 *of Climate*, 34, 5063–5080, <https://doi.org/10.1175/JCLI-D-20-0966.1>, 2021.

1223 Wu, Z., Jiang, C., Conde, M., Chen, J., and Deng, B.: The long-term spatiotemporal variability of sea  
1224 surface temperature in the northwest Pacific and China offshore, *Ocean Science*, 16, 83–97,  
1225 <https://doi.org/10.5194/os-16-83-2020>, 2020.

1226 Xiao, H.-W., Xiao, H.-Y., Luo, L., Shen, C.-Y., Long, A.-M., Chen, L., Long, Z.-H., and Li, D.-N.:  
1227 Atmospheric aerosol compositions over the South China Sea: temporal variability and source  
1228 apportionment, *Atmospheric Chemistry and Physics*, 17, 3199–3214, [https://doi.org/10.5194/acp-17-](https://doi.org/10.5194/acp-17-3199-2017)  
1229 [3199-2017](https://doi.org/10.5194/acp-17-3199-2017), 2017.

1230 Yost, C. R., Minnis, P., Sun-Mack, S., Chen, Y., and Smith, W. L.: CERES MODIS Cloud Product  
1231 Retrievals for Edition 4—Part II: Comparisons to CloudSat and CALIPSO, *IEEE Transactions on*  
1232 *Geoscience and Remote Sensing*, 59, 3695–3724, <https://doi.org/10.1109/TGRS.2020.3015155>, 2021.

1233 Yuan, C.-S., Chuang, H.-L., Tseng, Y.-L., Li, T.-C., Soong, K.-Y., and Cheng, W.-H.: Long-range  
1234 transport and source apportionment of marine fine particles in the Taiwan Strait and South China Sea  
1235 Intersection: Spatiotemporal variations and chemical fingerprints, *Atmospheric Environment*, 339,  
1236 120867, <https://doi.org/10.1016/j.atmosenv.2024.120867>, 2024.

1237 Yuan, T., Li, Z., Zhang, R., and Fan, J.: Increase of cloud droplet size with aerosol optical depth: An  
1238 observation and modeling study, *Journal of Geophysical Research: Atmospheres*, 113,  
1239 <https://doi.org/10.1029/2007JD008632>, 2008.

1240 Zhang, C., Xu, H., Li, Z., Xie, Y., and Li, D.: Maritime Aerosol Optical and Microphysical Properties in  
1241 the South China Sea Under Multi-source Influence, *Sci Rep*, 9, 17796, [https://doi.org/10.1038/s41598-](https://doi.org/10.1038/s41598-019-54483-6)  
1242 [019-54483-6](https://doi.org/10.1038/s41598-019-54483-6), 2019.

1243 Zhang, G. J., Ramanathan, V., and McPhaden, M. J.: Convection-Evaporation Feedback in the Equatorial  
1244 pacific, 1995.

1245 Zhang, Y. and Wang, K.: The Changing Morphology of Global Precipitation Systems during the Last  
1246 Two Decades, *Bulletin of the American Meteorological Society*, 105, E1861–E1880,  
1247 <https://doi.org/10.1175/BAMS-D-23-0106.1>, 2024.

1248 Zhao, C., Sun, Y., Yang, J., Li, J., Zhou, Y., Yang, Y., Fan, H., and Zhao, X.: Observational evidence  
1249 and mechanisms of aerosol effects on precipitation, *Science Bulletin*, 69, 1569–1580,  
1250 <https://doi.org/10.1016/j.scib.2024.03.014>, 2024.

1251 Zheng, B., Qu, J., Huang, Y., Peng, D., Gu, D., Li, C., and Huang, R.: Evaluating the Seasonal Cycle of  
1252 the South China Sea Monsoon in CMIP6 Models, *J Meteorol Res*, 39, 322–337,  
1253 <https://doi.org/10.1007/s13351-025-4170-x>, 2025.

1254 Zheng, H., Liu, M., Lohmann, R., Li, D., Vojta, S., Katz, S., Wang, W., Ke, H., Wang, C., and Cai, M.:  
1255 Gaseous polycyclic aromatic hydrocarbons over the South China Sea: Implications for atmospheric  
1256 transport under monsoon influences, *Marine Pollution Bulletin*, 191, 114982,  
1257 <https://doi.org/10.1016/j.marpolbul.2023.114982>, 2023.

1258 Zheng, X., Xi, B., Dong, X., Wu, P., Logan, T., and Wang, Y.: Environmental effects on aerosol–cloud  
1259 interaction in non-precipitating marine boundary layer (MBL) clouds over the eastern North Atlantic,  
1260 *Atmos. Chem. Phys.*, 22, 335–354, <https://doi.org/10.5194/acp-22-335-2022>, 2022.

1261 Zhu, S., Xiao, Z., Che, H., and Chen, Q.: Impact of aerosols on warm clouds over the Sichuan Basin,  
1262 China in winter based on the MERRA-2 reanalysis dataset, *Atmospheric Pollution Research*, 13, 101342,  
1263 <https://doi.org/10.1016/j.apr.2022.101342>, 2022.

1264 Zhu, S., Li, Z., Chen, M., Wen, Y., Gao, S., Zhang, J., Wang, J., Nan, Y., Ferraro, S. C., Tsoodle, T. E.,  
1265 and Hong, Y.: How has the latest IMERG V07 improved the precipitation estimates and hydrologic  
1266 utility over CONUS against IMERG V06?, *Journal of Hydrology*, 645, 132257,  
1267 <https://doi.org/10.1016/j.jhydrol.2024.132257>, 2024.

1268